PHYSICAL REVIEW D VOLUME 41, NUMBER 3 1 FEBRUARY 1990

Experimental study of the reactions $\bar{p}p \rightarrow \pi^- \pi^+$ and $K^- K^+$ between 360 and 760 MeV/c

T. Tanimori, S. Ishimoto, K. Nakamura,* and K. H. Tanaka
National Laboratory for High Energy Physics, Oho, Ibaraki 305, Japan

M. Sudou[†] and S. Homma
Institute for Nuclear Study, University of Tokyo, Tanashi, Tokyo 188, Japan

Y. Sugimoto[‡]
Department of Physics, Kyoto University, Kyoto 606, Japan

T. Fujii
Department of Physics, University of Tokyo, Tokyo 113, Japan
and Department of Physics, Kobe University, Kobe 657, Japan

Y. Fujii[‡]
Laboratory of Nuclear Science, Tohoku University, Sendai 982, Japan

S. Kohno,[§] Y. Morita,[‡] and Y. Sumi
Department of Physics, Hiroshima University, Hiroshima 730, Japan

(Received 14 August 1989)

The folded differential cross sections $d\sigma/d\Omega(\theta^*)+d\sigma/d\Omega(\pi-\theta^*)$, where θ^* is the center-of-mass angle of the negatively charged outgoing particle, have been measured for the reactions $\bar{p}p \rightarrow \pi^- \pi^+$ and $K^- K^+$ at 15 incident beam momenta between 360 and 760 MeV/c with much better statistics than previous experiments. The total cross sections for these reactions, $\sigma_{\pi^-\pi^+}$ and $\sigma_{K^-K^+}$, have also been obtained by integrating the folded differential cross sections. The folded differential cross sections of both reactions show a similar behavior at all measured beam momenta, characterized by a prominent peak at $|\cos\theta^*|=1$. The cross section $\sigma_{\pi^-\pi^+}$ shows a smooth but rapidly decreasing behavior as the beam momentum increases up to 550 MeV/c, whereas $\sigma_{K^-K^+}$ shows a smooth and flat momentum dependence. These results are compared with some theoretical calculations based on nonrelativistic quark models. Although the shape of the folded differential cross section of the $\bar{p}p \rightarrow \pi^- \pi^+$ reaction is rather well reproduced by these models, that of the $\bar{p}p \rightarrow K^- K^+$ reaction, and, in particular, the prominent peak at $|\cos\theta^*|=1$ cannot be explained at all. The information from other experiments indicates that this discrepancy is most pronounced at the backward angles. Moreover, the momentum dependence of both $\sigma_{\pi^-\pi^+}$ and $\sigma_{K^-K^+}$ is not satisfactorily reproduced by these models.

I. INTRODUCTION

Hadrons are composed of quarks. In low-energy hadron reactions, however, it is difficult to analyze the dynamical aspects of the reaction mechanism in terms of the basic constituent interactions because many quarks and gluons are involved in the reaction. Among many hadron reactions, the $\bar{p}p$ annihilation is considered to be a good probe to study the complex feature of constituent interactions at low energies. Recently, a number of theoretical analyses for specific $\bar{p}p$ annihilation channels have been carried out based on nonrelativistic quark models.[1–13] For example, $\bar{p}p$ annihilation at rest into multipions has been analyzed in terms of the quark-rearrangement model.[1–4,6] Also, $\bar{p}p$ annihilation into two-meson final states has been analyzed in terms of the quark-antiquark-annihilation model and the quark-rearrangement model.[5,7–13]

Among the $\bar{p}p$ annihilation reactions, those into the two-meson final states have the following outstanding features which make explicit model calculations feasible: (i) the quantum numbers of these channels are strongly restricted by the selection rules; (ii) only two types of the quark-line diagrams, the rearrangement process [R process, Fig. 1(a)] and the annihilation process [A process, Fig. 1(b)], contribute.

Among various two-meson final states, the $\bar{p}p \rightarrow \pi^- \pi^+$ and $K^- K^+$ reactions are particularly important, since in these channels precise measurements of the angular distributions for annihilation in flight are possible and these distributions provide important information for quantitative understanding of the quark dynamics.[5,12] In particular, the $\bar{p}p \rightarrow K^- K^+$ reaction is possible only through the A process. Therefore detailed comparisons of both cross sections and the angular distributions between the $\bar{p}p \rightarrow \pi^- \pi^+$ and $\bar{p}p \rightarrow K^- K^+$ reactions offer possibilities

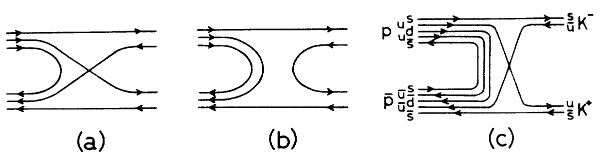

FIG. 1. (a) Diagram for the quark-rearrangement process (R process). (b) Diagram for the quark-annihilation process (A process). (c) Diagram proposed by Ellis, Gabathuler, and Karliner, which contributes to the $\bar{p}p \rightarrow K^- K^+$ backward peak via nonvalence $s\bar{s}$ quarks.

to study both the quark-rearrangement and the quark-annihilation mechanisms quantitatively.

Some issues in the recent theoretical analyses[5,7–13] for these channels are the following. (i) Which quark diagram is the dominant process? (ii) Which vertex, $^3P_0$ (vacuum quantum number) or $^3S_1$ (gluon quantum number), is important for the $\bar{q}q$ annihilation or creation? (iii) Below ~1 GeV/c, a backward peak exists in the $\bar{p}p \rightarrow K^- K^+$ reaction which is difficult to explain by nonrelativistic quark models with only the A process.[5,12]

An interesting possibility has been recently put forward regarding this last issue. The recent deep-inelastic polarized muon-proton scattering experiment by the European Muon Collaboration[14] (EMC) indicated that the proton spin cannot be completely given by the helicity of constituent quarks. This experimental result as well as various theoretical arguments suggests that baryons contain a significant amount of $s\bar{s}$ pairs.[15] Ellis, Gabathuler, and Karliner[16] argue that this explains the backward peak in the reaction $\bar{p}p \rightarrow K^- K^+$ at around 500 MeV/c, via the diagram shown in Fig. 1(c).

In order to resolve these questions, precise data on the momentum dependence of the cross sections and the angular distributions for both $\bar{p}p \rightarrow \pi^- \pi^+$ and $K^- K^+$ reactions are needed. However, high-statistics data for these reactions are available only at beam momenta above ~1 GeV/c (Refs. 17 and 18). Below ~1 GeV/c, there are limited experimental data.[19–23] In particular, below 0.7 GeV/c, only two bubble-chamber experiments with low statistics[19,21] and one counter experiment with rather wide beam-momentum steps (~100 MeV/c) (Ref. 22) have measured both $\bar{p}p \rightarrow \pi^- \pi^+$ and $K^- K^+$ reactions. An experiment[23] at CERN's Low Energy Antiproton Ring (LEAR) has also measured $\bar{p}p \rightarrow \pi^- \pi^+$ cross sections between 158 and 275 MeV/c. Although Tanimori *et al.*[22] presented the angular-distribution data with relatively good statistics, the quality of their data, in particular, for the $\bar{p}p \rightarrow K^- K^+$ reaction is not quite satisfactory for detailed theoretical analyses.

In view of the above situation we have measured the folded differential cross section $d\sigma/d\Omega(\theta^*)+d\sigma/d\Omega(\pi-\theta^*)$ and the integrated total cross section for the reactions $\bar{p}p \rightarrow \pi^- \pi^+$ and $K^- K^+$ at 15 incident beam momenta between 360 and 760 MeV/c, where θ^* is the center-of-mass angle of the negatively charged outgoing particle. In addition to the investigation of the reaction mechanism of the $\bar{p}p$ annihilation processes at the constituent level, there was another motivation in this experiment, i.e., the search for meson resonances formed by the $\bar{p}p$ system in the mass range between 1910 and 2000 MeV/c^2, or particularly in the S-resonance region (~1936 MeV/c^2). The latter results have already been published elsewhere.[24] In this paper we present the full description of the experiment and the detailed results and discussion on the angular distribution data of the $\bar{p}p \rightarrow \pi^- \pi^+$ and $K^- K^+$ reactions.

II. EXPERIMENT

A. Experimental arrangement

Since our prime purpose was to measure the cross sections for the reactions $\bar{p}p \rightarrow \pi^- \pi^+$ and $K^- K^+$ as precisely as possible, the present experiment was designed to have the following features: (i) high selection efficiency for the $\pi^- \pi^+$ and $K^- K^+$ events; (ii) large and smooth acceptance (about $\frac{1}{6}$ of 4π sr). For this purpose no spectrometer magnet was used because the $\pi^- \pi^+$ and $K^- K^+$ events can be identified by using only the angular information between the incident $\bar{p}$ and the outgoing particles as described below. A definite advantage of the absence of magnetic field is that good angular and spatial resolutions for the charged-particle tracks can be obtained easily, which enables one to distinguish both $\pi^- \pi^+$ and $K^- K^+$ events clearly from huge amounts of the background events, and to reduce the systematic errors significantly. Another advantage is that a large and smooth acceptance can be obtained, which is also very important in reducing both systematic and statistical errors. However, since the charge of the outgoing particles cannot be determined with this method, we have obtained only the folded differential cross section $(d\sigma/d\Omega)(\theta^*)+(d\sigma/d\Omega)(\pi-\theta^*)$. A plan view of the experimental arrangement is shown in Fig. 2.

The antiproton beam was provided by the K4 beam channel at the KEK 12-GeV Proton Synchrotron. The K4 has a double-stage electrostatic separator and transports high-quality antiproton beams in the momentum range between 400 and 800 MeV/c (Ref. 25). The beam intensity per 10^{12} primary protons of 12 GeV impinging on a 60-mm-long platinum target was about 1000 antiprotons at 700 MeV/c, and decreased to about 40 antiprotons at 400 MeV/c. The momentum bite of the beam was ±3.0%. At the final focus, the beam size (rms) was typically 14 mm in the horizontal and 10 mm in the vertical directions. The $\bar{p}/\pi^-$ ratio was typically $\frac{1}{3}$ above 480 MeV/c, but decreased to about $\frac{1}{15}$ at 400 MeV/c.

The liquid-hydrogen target was 20 cm long and 8 cm in diameter. The target flask was made of 150-μm-thick stainless-steel cylinder with 350-μm-thick spherically shaped Mylar caps at both ends. The target was placed at the center of a 28-cm-diameter vacuum chamber having 250-μm-thick large Mylar windows. The density of liquid hydrogen was monitored by measuring its vapor pressure. It was 1.05±0.05 atm, and the corresponding density was 0.0706±0.0002 g/cm^3.

Five trigger scintillation counters C1–C5 were placed

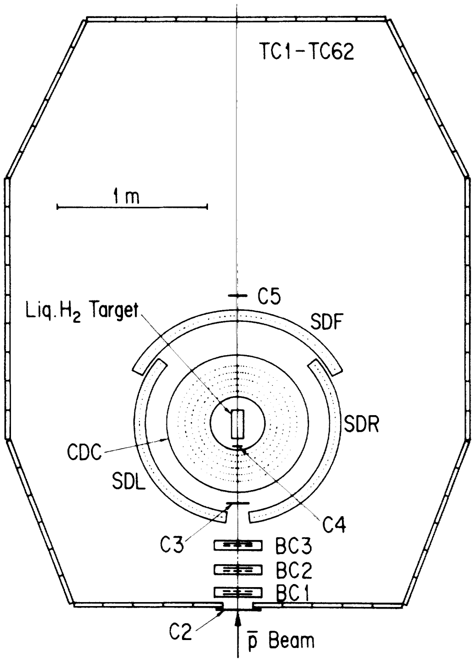

FIG. 2. Plan view of the experimental apparatus. C2–C5, trigger counters; BC1–BC3, multiwire proportional chambers of bidimensional readout; CDC, five-layer cylindrical drift chamber; SDL, SDF, and SDR, semicylindrical drift chambers with cathode readout; TC1–TC62, trigger-counter hodoscopes. The counter C1 (located about 5 m upstream of C2) and the shower counters (gamma counters) are not shown.

along the beam line in order to identify the antiproton beam. The counters C2 and C3 were viewed by two photomultiplier tubes from both ends to obtain good time resolutions. The circular counter C4 with a 7-cm diameter was located just upstream of the liquid-hydrogen target, and defined the beam spot well inside the target volume. The antiproton beam was identified at the trigger level by using timing and pulse-height information from the counters C1–C4. Noninteracting antiprotons were vetoed by the circular counter C5 with a 12-cm diameter. In the off-line analysis, the residual pion contamination was checked by inspecting the time-of-flight between and the pulse heights of C2 and C3, and negligible contamination (less than 0.02%) was found.

Two sets of shower counters called "gamma counters" (not shown in Fig. 2) were placed about 40 cm above and below the liquid-hydrogen target. Each set consisted of eight shower counter modules of lead-scintillator sandwich structure. These counters were used to veto γ rays from π^0 decay as well as charged particles produced in multipion annihilation reactions.

A multilayer cylindrical drift chamber (CDC), placed just outside the target vacuum chamber, was used as a main tracking detector. It was described in detail in Ref. 26. The CDC consisted of five concentric layers with radii ranging from 22 to 39.6 cm. The height of the active area was 30 cm. Each layer had two different types of drift cells: small cells with a drift length of 17.28 mm and large cells with that of 34.56 mm. There were a total of 96 small cells and 232 large cells. Since all the wires were strung in parallel, the CDC provided the coordinates of hit positions projected onto the horizontal plane. The trajectory of the beam antiproton was measured by three sets of multiwire proportional chambers of bidimensional readout, BC1–BC3, and the CDC.

Outside of the CDC were placed three semicylindrical drift chambers (SDC's), SDR, SDF, and SDL, with cathode strips running orthogonal to the sense wires. They provided horizontal and vertical coordinates of the hit positions of the outgoing particles. The chambers SDR and SDL had an identical structure with a radius of curvature of 65 cm, while SDF had a little larger radius of curvature (75 cm) in order to have an overlap region with SDR and SDL. Three SDC's as well as the CDC were placed concentrically. The unit cell of all the SDC's subtended the same azimuthal angle of 2.64° with respect to the concentric center. Each SDC covered an azimuthal angle of 121.44° with 46 drift cells, and had a height of 46 cm with 45 horizontal cathode strips each 8 mm wide and 2 mm apart. Further details of the SDC's are given in Ref. 27.

A trigger-counter hodoscope, consisting of 62 scintillation counters, surrounded the target and the other detectors to provide a trigger signal for an event having more than two final-state charged particles. The heights of scintillators were 100 cm for the backward 10 counters, 120 cm for the middle 30 counters, and 150 cm for the forward 22 counters. The width and the thickness were, respectively, 20 and 3 cm for all the counters. Each counter was viewed by two photomultiplier tubes (PMT's). The time difference between the top and the bottom PMT pulses provided the vertical coordinate of a hit particle with a rms resolution of about 6 cm.

B. Trigger

The trigger logic is schematically shown in Fig. 3. For the trigger condition (master trigger), the basic requirements were the existence of an incident antiproton and two or more outgoing charged particles, and no hit in the gamma counters.

The incident antiproton was identified by the coincidence $C1\cdot C2\cdot C3\cdot C4$ with delays and attenuators adjusted to the antiproton. This coincidence was vetoed by inhibit signals due to the data-acquisition dead time and the discharge of electrostatic separators. It is called gated $\bar{p}$ and simply represented by $C1\cdot C2\cdot C3\cdot C4$ hereafter. The number of the gated $\bar{p}$ signal provided the beam normalization. In order to veto noninteracting antiprotons, $(C1\cdot C2\cdot C3\cdot C4)\cdot\overline{C5}$ was formed. This provided the start signal for time-to-digital converters (TDC's) and the gate signal for coincidence registers (CR's). When this signal was generated but the master-trigger condition was not satisfied, the TDC's and the CR's were fast-cleared within 2 μs.

The master trigger was defined by $(C1\cdot C2\cdot C3\cdot C4)\cdot\overline{C5}\cdot\overline{G}\cdot T$. The logic signal G was defined as the logical OR of 16 γ-counter modules. The logic signal T was constructed as follows. The outputs of the two PMT's of each element of the trigger-counter hodoscopes

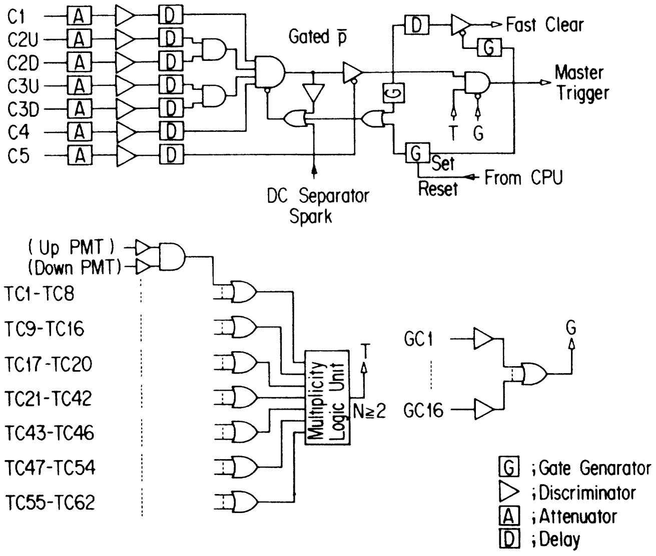

FIG. 3. Block diagram showing the trigger logic.

were fed to a coincidence circuit via discriminators. The coincidence signal from each trigger counter was then connected to a logic OR circuit. The trigger-counter hodoscopes were divided into seven groups, and the logical OR was constructed for each of these groups. The outputs of seven groups of logical OR circuits were then sent to a multiplicity logic unit (MLU). The logic signal T, i.e., the output of the MLU, was generated when two or more inputs out of seven were active. Each group of counters subtended an angle less than 90° with respect to the target center so as not to cause a trigger bias for both the $\bar{p}p \rightarrow \pi^- \pi^+$ and $K^- K^+$ events, which have an opening angle larger than 135° and 130°, respectively. Once the master trigger was generated, the trigger logic was disabled by inhibiting the gated $\bar{p}$ during the data acquisition, until a reset signal was issued by the CPU.

C. Experimental procedure

The measurement has been performed in the beam momentum region between 360 and 760 MeV/c with a momentum step of less than 50 MeV/c. The data taking was carried out at 15 beam-momentum settings in nearly random order, so that possible long-term time-dependent systematic errors did not contribute to make spurious structures in the momentum dependence of the cross sections. Typically 2000 $\pi^- \pi^+$ events and 300 $K^- K^+$ events were collected at each beam momentum. At the lowest beam momentum of 362 MeV/c, the number of the collected events was about a half of that at other momenta due to the low beam intensity.

The data was also taken with the target empty for estimating the effect of the wall of the target flask. In addition, the data were recorded with several trigger modes other than the normal trigger: for example, (i) antiproton-beam trigger (C1·C2·C3·C4) for studying the beam quality and the trigger efficiency and (ii) pion beam trigger (timings and attenuations of C1–C4 adjusted to the pions) for checking the detector response to minimum-ionizing particles.

The data acquisition was controlled by a PDP-11/73 computer and a system of encoder and buffer-memory modules developed at KEK (Ref. 28). Digitized data from CAMAC modules were encoded and compressed by an encoder module. The encoded data were transferred to a buffer-memory module installed in a main CAMAC crate. The computer had access only to the main crate in which the buffer-memory modules and some other CAMAC modules for trigger decision were installed. The data size was about 120 words per event, and the present data-acquisition system was able to record about 30 events per beam spill. The dead time was about 5% at the lowest beam momentum and about 30% at the highest.

The on-line analysis was executed for sampled events for the purpose of monitoring the performance of the detectors and electronics. At the same time, the off-line analysis for checking the recorded data was carried out with the KEK central computer HITAC M280H.

III. ANALYSIS OF DATA

A. Event reconstruction

The horizontal projection of the charged-particle track was reconstructed by using the CDC and SDC's. The three SDC's and the CDC were placed with their common cylinder axis vertically traversing the center of the target, and the structure of the drift cells of the SDC's was the same as that of the large cells of the CDC. Therefore, the anode layers of the SDC's were treated as if they were the sixth and seventh layers of the CDC in the horizontal track reconstruction. The track-finding algorithm was based on the link-and-tree method.[29] The reconstructed track was required to have at least four hits. When two or more track candidates were found, the one which gave a minimum "χ^2 of linear fit" was adopted.

The beam track was independently reconstructed by using the CDC and the beam chambers BC1–BC3. These two reconstructed tracks were required to coincide within ±6 mm on the C3 plane and to have the directions consistent with each other within ±30 mrad. The vertical direction of the beam track was reconstructed by using only the beam chambers. The reconstruction efficiency for the beam track was dependent on the beam momentum, and was found to be 94.8–96.6% with an estimated error of ±1.0%.

In the next step we selected the events in which one beam track and two outgoing charged-particle tracks were reconstructed in the horizontal plane. A weighted mean of the two intersections between the beam track and two outgoing tracks was adopted as the vertex point in the horizontal plane. The weight used here was $\sin^2\theta$, where θ is an angle between the beam track and an outgoing track projected onto the horizontal plane. The vertical coordinate of the vertex point was determined by extrapolating the beam track to the vertex point.

The three-dimensional reconstruction of the outgoing tracks was performed for those events as selected above. The vertical coordinates of the outgoing tracks were obtained from the induced-charge distributions on the cathode strips of the SDC's. When two or more candidates for the hit points on the SDC cathode were found corresponding to one track, the vertical hit position on the trigger-counter hodoscope was examined and the most consistent one with the trigger counter was chosen.

The inefficiency of the horizontal track reconstruction in the drift chambers was mainly caused by (i) tracking inefficiency due to the inefficiencies of the drift chambers, (ii) loss of events due to wrong tracking (wrong choice of left-right twins of the drift-chamber hits), and (iii) loss of events due to spurious tracks caused by either cross talk or electric noise. To study the inefficiency due to (i), it was examined by using multipion events whether a track reconstructed by the CDC and SDC's was consistent with a track reconstructed from the hit points on the SDC and the trigger-counter hodoscope. From this study the tracking inefficiency was found to be (0.8±0.15)% for one track. The inefficiencies due to (ii) and (iii) were determined by visual inspection of one-event displays. At each beam momentum, 1200 event samples were visually scanned, and the loss of events was estimated to be (1.0±0.4)% due to wrong tracking and (0.2±0.1)% due to spurious tracks. The reconstruction efficiency in the vertical direction was estimated to be (97.4±1.3)% from the efficiency (~99%) of the cathode readout of the SDC's. The overall reconstruction efficiency for the two outgoing particles was estimated to be (94.7±1.4)% at all beam momenta by combining the efficiencies described above.

B. Selection of two-body mesonic reactions

The data-summary tapes (DST's) were produced in two stages. Events selected at the first stage were required to have a beam track reconstructed by beam chambers in both horizontal and vertical directions, and three or four tracks (including the beam track) reconstructed by drift chambers in the horizontal plane. At this stage, a beam track was not linked with a track in the CDC yet. The events with four drift-chamber tracks were reserved for a study of accidental hits and cross talk.

At the second stage the events of two-body mesonic reactions ($\bar{p}p \rightarrow \pi^-\pi^+$ and $\bar{p}p \rightarrow K^-K^+$) were selected. The first requirement for such events was to have three reconstructed tracks. The $\bar{p}p$ elastic-scattering events were rejected by examining an opening angle between the two outgoing tracks. The events with an opening angle less than 95° or greater than 200° were discarded because the elastic event has an opening angle of approximately 90°, while the $\pi^-\pi^+$ and K^-K^+ events have the opening angle between about 130° and 180°. The events having three tracks (two outgoing particles) include a huge amount of background from multipion annihilation events such as $\bar{p}p \rightarrow \pi^+\pi^-\pi^0$, $\pi^+\pi^-\pi^0\pi^0$, etc. These multipion background events were reduced by applying a coplanarity cut. Figure 4 shows examples of the distributions of the acoplanarity angle θ_{acop} which is defined as an angle between the plane determined by two tracks and the remaining track. The peak at $\theta_{\text{acop}}=0$ corresponds to the events of two-body mesonic reactions. The elastic events are not included in this figure because they were already rejected by the opening-angle cut.

To finally retain the two-body mesonic-reaction candidates in the second-stage DST's, the cut on the acoplanarity-angle distribution was chosen as $\theta_{\text{cut}}=3\sigma+15$ mrad, where σ is a rms width of the coplanarity peak. The value of σ was dependent on the beam momentum because it was determined mainly by the multiple scattering of antiprotons at the counter C3. The value of θ_{cut} was 51 mrad at the highest beam momentum and 72 mrad at the lowest. This rather loose cut was adopted so as not to lose the $\pi^-\pi^+$ and K^-K^+ events. It was confirmed that this coplanarity cut caused no significant loss of the $\pi^-\pi^+$ and K^-K^+ events from the following facts: (i) the events excluded by the coplanarity requirement did not make peaks in the $R_{\pi K}$ distribution corresponding to the $\pi^-\pi^+$ and K^-K^+ events (see Sec. III C); (ii) the cross sections $\sigma_{\pi^-\pi^+}$ and $\sigma_{K^-K^+}$ did not change significantly when the value of $|\theta_{\text{cut}}|$ was increased.

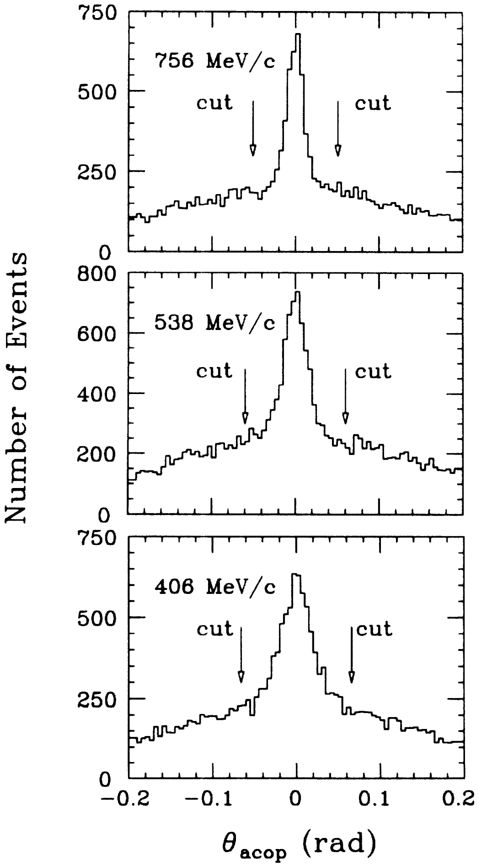

FIG. 4. Acoplanarity-angle distributions at beam momenta of 406, 538, and 756 MeV/c. The positions of the cuts are also shown.

C. Selection of $\bar{p}p \to \pi^-\pi^+$ and K^-K^+ events

In order to distinguish between the $\pi^-\pi^+$ and K^-K^- events, the opening angle between the two outgoing particles was examined in detail. From the two-body kinematics, the opening angle is uniquely determined when the four-momentum of the incident antiproton, the direction of one of the outgoing particles, and the masses of the two outgoing particles are given. The difference between the predicted opening angles for the $\pi^-\pi^+$ and K^-K^+ events is shown in Fig. 5 as a function of $\cos\theta^*$.

Figure 6 shows an example of the distribution of $\Delta\theta_{\pi\pi}$ for the events satisfying the coplanarity requirement, where $\Delta\theta_{\pi\pi}$ means the difference between the measured opening angle and the one predicted from the $\bar{p}p \to \pi^-\pi^+$ kinematics. The energy loss of the incident antiproton in the liquid-hydrogen target down to the vertex point was included in the calculation of the predicted opening angle. The prominent peak in this figure corresponds to the $\pi^-\pi^+$ events, while the K^-K^+ events cluster at the left-side tail of the $\pi^-\pi^+$ peak. The width of the $\Delta\theta_{\pi\pi}$ distribution is about 7 mrad, which is consistent with the combined contributions from the beam-momentum spread and multiple scattering of the outgoing particles.

The K^-K^+ events are not well separated from the $\pi^-\pi^+$ events in Fig. 6, because the opening-angle difference between the $\pi^-\pi^+$ and K^-K^+ events varies with the scattering angle. In order to achieve clear separation between the $\pi^-\pi^+$ and K^-K^+ events, we define a variable $R_{\pi K}$ as

$$R_{\pi K} = \frac{\theta_{\text{open}} - \theta_{KK}}{\theta_{\pi\pi} - \theta_{KK}} ,$$

where θ_{open} is the measured opening angle and θ_{KK} and $\theta_{\pi\pi}$ are the predicted opening angles for the K^-K^+ and $\pi^-\pi^+$ events, respectively. Figure 7 shows examples of

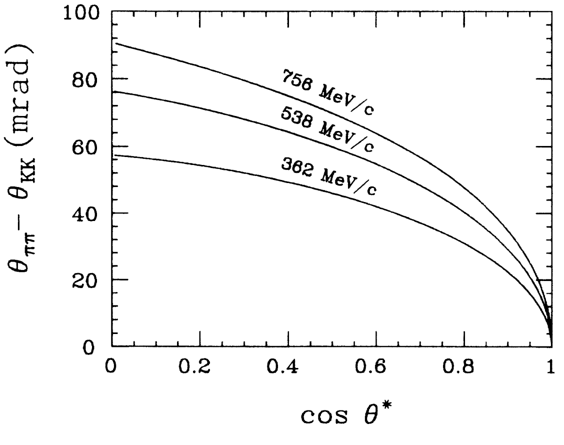

FIG. 5. The difference between the opening angles for the reactions $\bar{p}p \to \pi^-\pi^+$ and $\bar{p}p \to K^-K^+$ at several beam momenta. Here, θ^* is the c.m. angle of the K^-K^+ reaction, and the opening angles are compared for the kinematical condition that the backward-going particles from the $\pi^-\pi^+$ and K^-K^+ reactions have the same laboratory angle.

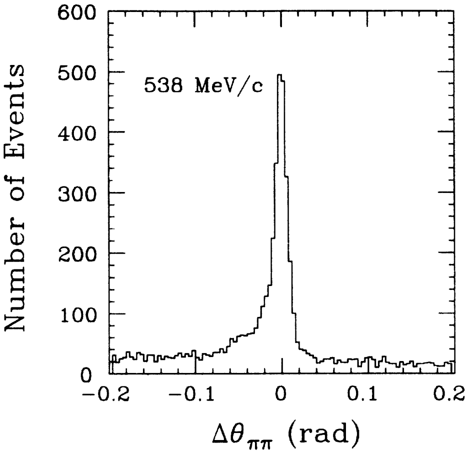

FIG. 6. $\Delta\theta_{\pi\pi}$ distribution at 538 MeV/c, where $\Delta\theta_{\pi\pi}$ is the difference between the measured and predicted opening angles for the $\bar{p}p \to \pi^-\pi^-$ reaction.

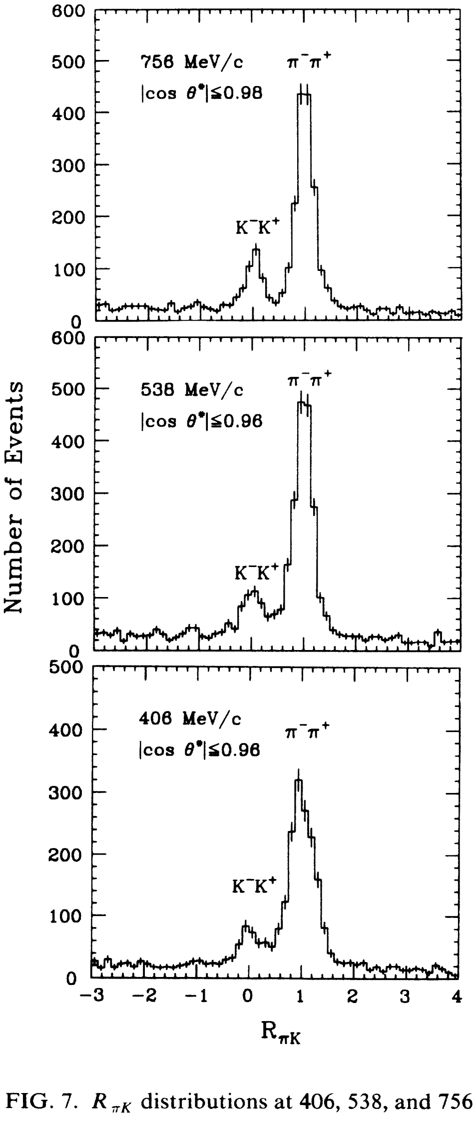

FIG. 7. $R_{\pi K}$ distributions at 406, 538, and 756 MeV/c.

the $R_{\pi K}$ distribution for the events satisfying the coplanarity requirement. The $K^- K^+$ events clustering around $R_{\pi K}=0$ are now clearly separated from the $\pi^-\pi^+$ events clustering around $R_{\pi K}=1$.

To ascertain the performance of this $\pi^-\pi^+/K^-K^+$ separation, the pulse height of the trigger-counter hodoscope for the backward-going particle was inspected at an incident beam momentum of 756 MeV/*c*. At this beam momentum, the backward-going particle from the $\bar{p}p \to K^-K^+$ reaction should have about a 1.8-times-larger pulse height than that from the $\bar{p}p \to \pi^-\pi^+$ reaction (the momentum of the backward-going particle with $\theta_{\text{lab}} > 145°$ is ~ 560 MeV/*c* for the K^-K^+ channel and ~ 700 MeV/*c* for the $\pi^-\pi^+$ channel at this beam momentum). A scatter plot of $R_{\pi K}$ versus pulse height of the trigger-counter hodoscope for the backward-going particles (10 backward counters were used) is shown in Fig. 8(a). The pulse-height distribution for the K^-K^+ region ($-0.3 < R_{\pi K} < 0.3$) and that for the $\pi^-\pi^+$ region ($0.7 < R_{\pi K} < 1.3$) are shown in Fig. 8(b). It can be seen from these figures that particles around $R_{\pi K}=0$ clearly have larger pulse heights than those around $R_{\pi K}=1$.

It should be mentioned here that after selecting the events of two-body mesonic reactions, two additional requirements were imposed on the data. One was a cut for the vertex position in order to eliminate the spurious events caused by the interaction in C4. The hit pattern of the trigger-counter hodoscope was also required to be consistent with the drift-chamber tracks in the horizontal plane.

In order to obtain the angular distributions of the $\pi^-\pi^+$ and K^-K^+ events, the center-of-mass angles were subdivided into typically 20 bins in $|\cos\theta^*|$ for the $\bar{p}p \to \pi^-\pi^+$ reaction and 10 bins for the $\bar{p}p \to K^-K^+$ reaction. In each $|\cos\theta^*|$ bin, the $R_{\pi K}$ distribution was fitted with a superposition of a linear background term and two Gaussian peaks, as shown in Fig. 9. The same width was used in the fit for the two peaks because the opening-angle resolution was the same for the $\pi^-\pi^+$ and K^-K^+ channels. The number of events in each $R_{\pi K}$ bin was then divided into $\pi^-\pi^+$, K^-K^+, and background in proportion to the respective contributions in that $R_{\pi K}$ bin determined by the fit.

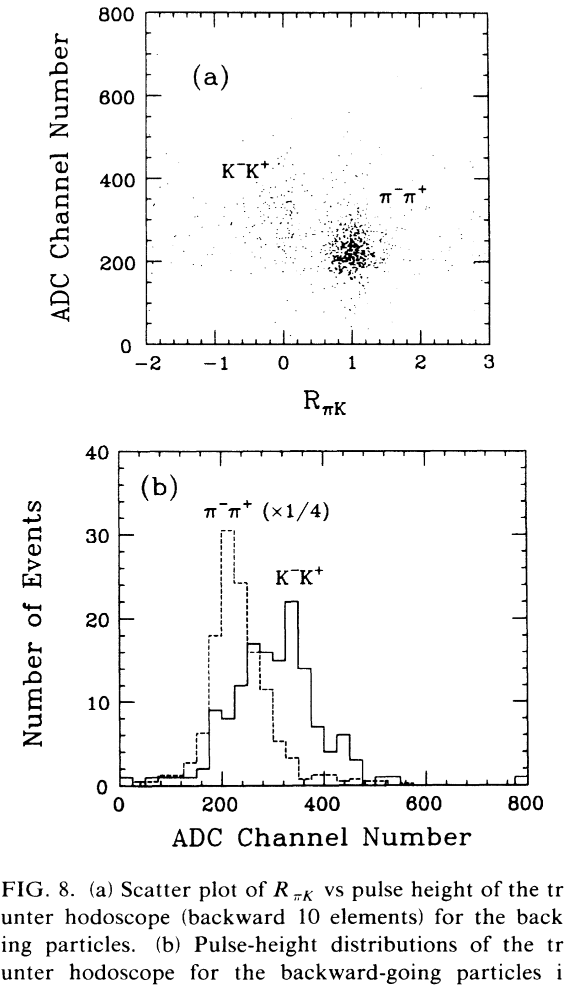

FIG. 8. (a) Scatter plot of $R_{\pi K}$ vs pulse height of the trigger-counter hodoscope (backward 10 elements) for the backward-going particles. (b) Pulse-height distributions of the trigger-counter hodoscope for the backward-going particles in the K^-K^+ region ($-0.3 < R_{\pi K} < 0.3$) and in the $\pi^-\pi^+$ region ($0.7 < R_{\pi K} < 1.3$). The data at a beam momentum of 756 MeV/*c* were used for both (a) and (b).

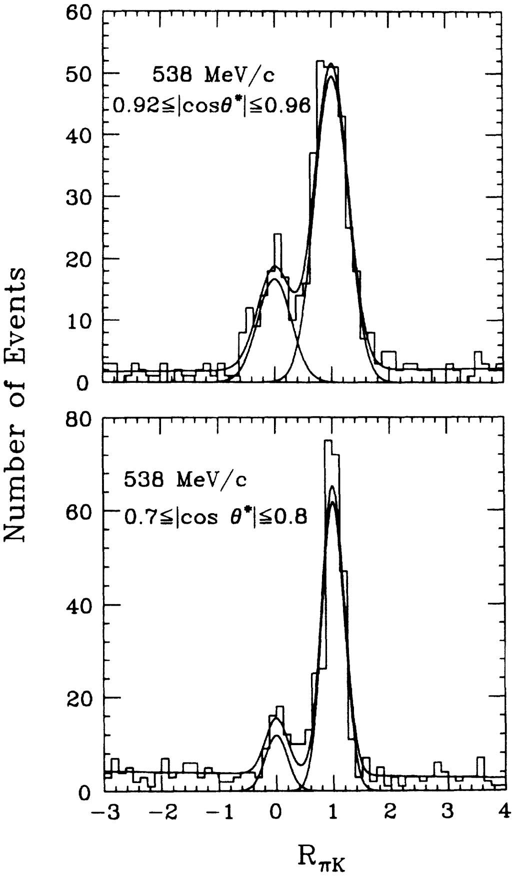

FIG. 9. Examples of the $R_{\pi K}$ distribution for subdivided intervals of $|\cos\theta^*|$. The curves show the results of the fit with a sum of two Gaussian peaks and linear background. Two Gaussian peaks are also shown.

D. Acceptance calculation and decay correction

The acceptance at each beam momentum was calculated by a Monte Carlo method in which the beam phase space and the beam-momentum spread were represented by Gaussian distributions determined by the actual data. The energy loss due to the liquid-hydrogen target was also taken into account. The outgoing kaons were allowed to decay. The decay modes of $K^\pm\to\mu^\pm\nu$, $\pi^\pm\pi^0$, $\pi^\pm\pi^\pm\pi^\mp$, $\pi^\pm\pi^0\pi^0$, $\pi^0\mu^\pm\nu$, and $\pi^0e^\pm\nu$ were taken into account, but the other decay modes with branching ratios of less than 1% were ignored. It was found that about 40% of K^-K^+ events had one or two kaons which decayed before reaching the trigger-counter hodoscope. However, not all of them were lost. The daughter particle of the decayed kaon was further traced to determine whether or not the event was accepted. When any of the gamma counters was hit by a γ or a charged pion, that event was not accepted. Events in which a kaon decayed before the outermost layer of the CDC with a decay angle larger than 20 mrad in the laboratory frame were not regarded as the K^-K^+ event because they were considered to be eliminated by the coplanarity cut or to fall outside of the K^-K^+ region in the $R_{\pi K}$ distribution.

The acceptance including the decay loss is shown in Fig. 10 as a function of $|\cos\theta^*|$. The total acceptance was about 3.0 sr for the $\pi^-\pi^+$ events and about 2.2 sr for the K^-K^+ events. The acceptance was found to have only a little dependence on the beam momentum.

To estimate the acceptance uncertainty due to the positioning error of the apparatus, the acceptance was calculated by a Monte Carlo program in which the positions of all the detector elements were moved within maximum possible positioning errors. From this study, the acceptance uncertainty was estimated to be ±0.7% for both the $\pi^-\pi^+$ and K^-K^+ events.

TABLE I. Summary of the normalization corrections and systematic errors.

Origin	Correction (%)	Error (%)
Beam reconstruction efficiency	94.8–96.6	±1.0
Beam absorption	5.4–8.2	±0.4
Reconstruction efficiency for the two outgoing particles	94.7	±1.4
Absorption of outgoing particles	2.5[a] 2.9[b]	±0.2[a]±0.6[b]
Effective target length		±0.8
Target density		±0.3
Acceptance uncertainty		±0.7
Total systematic error		±2.1[a]±2.2[b]

[a] For the $\bar{p}p\to\pi^-\pi^+$ reaction.
[b] For the $\bar{p}p\to K^-K^+$ reaction.

E. Other corrections

The number of protons in the target was determined from the effective target length and density (0.0706±0.0002 g/cm^3) of liquid hydrogen. The effective target length was defined as an averaged path length of unscattered beam tracks in the liquid-hydrogen target. It was (20.25±0.17) cm at all beam momenta, where an error due to the variation of the elasticity of Mylar at the liquid-hydrogen temperature was included. Therefore, the systematic errors concerning the number of target protons were ±0.8% due to the uncertainty in the effective target length and ±0.3% due to the uncertainty in the target density.

The absorption of antiprotons in liquid hydrogen was estimated in the following way. After having passed through liquid hydrogen of thickness x, the beam intensity $I(x)$ is given by

$$I(x)=I_0\exp(-\rho N_A\sigma_a x) \ ,$$

where I_0 is the intensity of the incident antiproton beam, ρ the density of liquid hydrogen, N_A the Avogadro number, and σ_a the cross section relevant to the $\bar{p}$ disappearance from the beam. The effective intensity $\bar{I}$ is given by

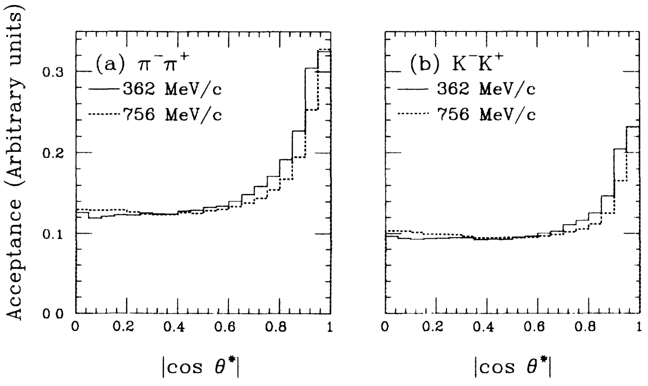

FIG. 10. Acceptance (including decay correction) as a function of $|\cos\theta^*|$ at the lowest and the highest beam momenta for (a) the $\bar{p}p\to\pi^-\pi^+$ reaction and (b) the $\bar{p}p\to K^-K^+$ reaction.

TABLE II. Summary of the absolute beam momentum at the target center ($P_{\rm lab}$), momentum spread ($\Delta P_{\rm lab}$), mass of the $\bar{p}p$ system ($M_{\bar{p}p}$), and mass resolution ($\Delta M_{\bar{p}p}$) at each measured point.

$P_{\rm lab}$ (MeV/c)	$\Delta P_{\rm lab}$ (FWHM) (MeV/c)	$M_{\bar{p}p}$ (MeV/c^2)	$\Delta M_{\bar{p}p}$ (FWHM) (MeV/c^2)
362	85	1910.0	15.0
406	64	1918.2	12.3
447	51	1926.5	10.7
467	47	1930.7	10.1
482	44	1934.0	9.7
495	42	1936.9	9.5
501	41	1938.3	9.4
522	39	1943.1	9.2
538	38	1946.9	9.2
559	37	1952.0	9.2
585	37	1958.5	9.4
628	37	1969.7	9.8
677	38	1983.0	10.6
718	40	1994.5	11.3
756	41	2005.5	12.1

$$\bar{I}=\frac{1}{l}\int_0^l I(x)dx=\frac{I_0}{\rho N_A\sigma_a l}[1-\exp(-\rho N_A\sigma_a l)]\ ,$$

where l is the effective target length. It should be noted that the beam antiprotons elastically scattered in the forward direction are not always lost from the beam. A Monte Carlo simulation shows that the relevant cross section for σ_a is the $\bar{p}p$ total cross section minus 10 mb. The beam absorption $1-\bar{I}/I_0$ was then estimated to be $(7.9\pm0.4)\%$ at the lowest beam momentum and $(5.1\pm0.4)\%$ at the highest. In addition, there was a small amount of beam absorption by the counter C4, which was estimated to be $(0.3\pm0.03)\%$ at all momenta.

The loss of events caused by absorption of the outgoing particles in the detector materials was estimated by a Monte Carlo simulation. It was found that there was no significant dependence of the correction on the direction of the outgoing particle and the momentum of the incident beam. Conservatively, the correction factor was estimated to be $(2.5\pm0.2)\%$ for the $\pi^-\pi^+$ events and $(2.9\pm0.6)\%$ for the K^-K^+ events.

A summary of the correction factors and the systematic errors is listed in Table I. The total systematic error is obtained by summing up all the contributions quadratically. It is $\pm2.1\%$ for the $\bar{p}p\to\pi^-\pi^+$ reaction and $=\pm2.2\%$ for the $\bar{p}p\to K^-K^+$ reaction.

F. Absolute beam momentum and mass resolution

The beam momentum at the target center was calibrated by exploiting the two-body kinematics of the

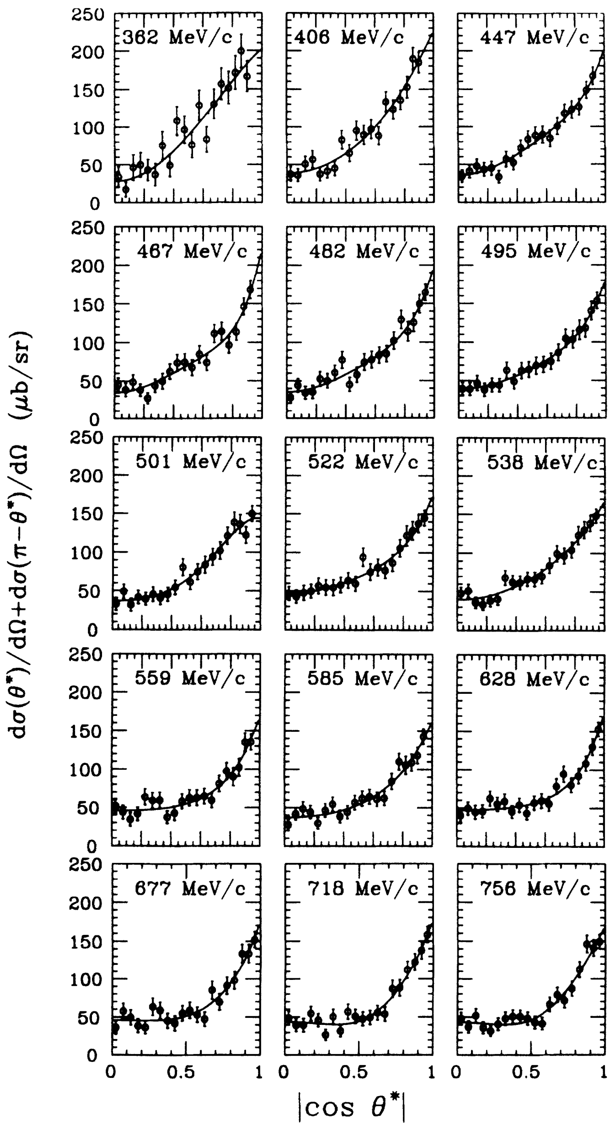

FIG. 11. Folded differential cross sections for the $\bar{p}p\to\pi^-\pi^+$ reaction. Curves are the results of the Legendre-polynomial fit.

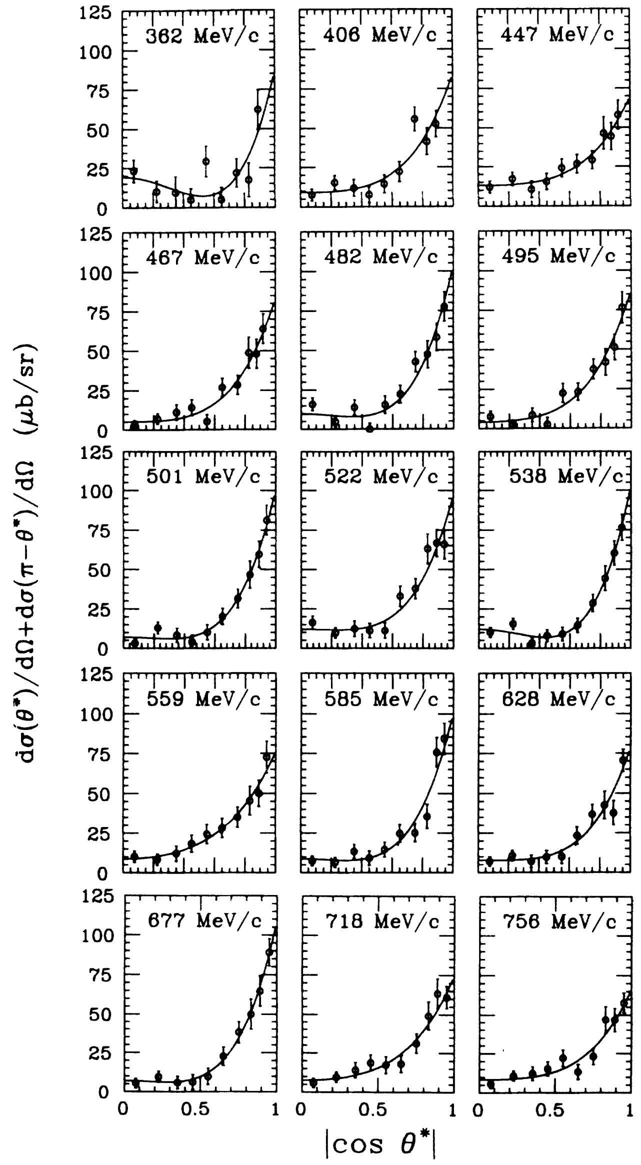

FIG. 12. Folded differential cross sections for the $\bar{p}p\to K^-K^+$ reaction. Curves are the results of the Legendre-polynomial fit.

TABLE III. Folded differential cross sections (FDC) for the $\bar{p}p\rightarrow\pi^-\pi^+$ reaction.

362 MeV/c		406 MeV/c	
$\lvert\cos\theta^*\rvert$	FDC (μb/sr)	$\lvert\cos\theta^*\rvert$	FDC (μb/sr)
0.025	33.9±13.1	0.025	37.5±9.5
0.075	17.1±9.6	0.075	36.3±8.4
0.125	46.2±17.0	0.125	51.2±10.1
0.175	49.9±16.2	0.175	57.2±11.3
0.225	42.9±13.9	0.225	37.8±9.1
0.275	36.8±14.7	0.275	41.6±9.1
0.325	74.9±18.7	0.325	45.3±9.6
0.375	48.9±14.7	0.375	82.8±12.4
0.425	107.7±19.4	0.425	65.3±11.0
0.475	95.9±18.0	0.475	95.0±12.6
0.525	75.9±16.8	0.525	89.3±12.6
0.575	128.5±20.1	0.575	96.9±12.5
0.625	83.3±16.7	0.625	88.0±11.9
0.675	130.2±19.7	0.675	133.4±13.4
0.725	156.6±20.7	0.725	123.2±12.8
0.775	151.4±21.3	0.775	135.7±13.0
0.820	171.2±21.8	0.820	152.6±14.2
0.860	199.4±21.8	0.860	189.4±14.7
0.900	166.4±19.9	0.900	184.7±13.5

447 MeV/c		467 MeV/c	
$\lvert\cos\theta^*\rvert$	FDC (μb/sr)	$\lvert\cos\theta^*\rvert$	FDC (μb/sr)
0.025	34.6±8.2	0.025	45.2±8.9
0.075	41.0±8.7	0.075	38.3±9.0
0.125	47.8±9.4	0.125	48.6±9.5
0.175	43.6±8.9	0.175	38.1±8.1
0.225	45.2±9.2	0.225	27.1±7.4
0.275	33.7±8.2	0.275	43.7±8.7
0.325	57.0±10.1	0.325	49.7±10.1
0.375	52.3±9.7	0.375	62.3±9.9
0.425	71.5±10.5	0.425	73.6±10.9
0.475	83.2±11.3	0.475	74.5±10.9
0.525	88.3±11.3	0.525	67.3±10.3
0.575	89.3±11.4	0.575	84.7±11.3
0.625	84.4±11.2	0.625	73.9±10.2
0.675	100.4±11.2	0.675	111.4±11.8
0.725	117.5±12.1	0.725	114.2±11.7
0.775	122.7±11.8	0.775	96.6±10.8
0.825	126.2±11.3	0.825	113.6±11.1
0.875	148.7±11.1	0.875	146.5±11.1
0.920	167.2±11.5	0.920	168.5±11.6

482 MeV/c		495 MeV/c	
$\lvert\cos\theta^*\rvert$	FDC (μb/sr)	$\lvert\cos\theta^*\rvert$	FDC (μb/sr)
0.025	27.9±7.3	0.025	39.1±8.3
0.075	43.9±8.9	0.075	38.8±8.6
0.125	34.1±8.4	0.125	46.7±9.8
0.175	35.2±8.8	0.175	37.9±8.8
0.225	52.6±9.7	0.225	44.1±9.2
0.275	50.0±9.4	0.275	43.8±8.9
0.325	60.6±9.9	0.325	63.5±10.6
0.375	77.3±11.0	0.375	48.8±9.5
0.425	45.1±9.1	0.425	63.0±10.6
0.475	57.9±9.8	0.475	64.6±10.1
0.525	74.3±10.7	0.525	69.6±11.0
0.575	77.5±10.9	0.575	70.8±10.5
0.625	83.3±10.9	0.625	74.9±10.5
0.675	85.0±10.6	0.675	86.4±10.9

TABLE III. (*Continued*).

	482 MeV/c		495 MeV/c
$\lvert\cos\theta^*\rvert$	FDC (μb/sr)	$\lvert\cos\theta^*\rvert$	FDC (μb/sr)
0.725	102.1±11.1	0.725	104.7±11.6
0.775	129.2±11.9	0.775	103.4±11.1
0.820	114.1±12.6	0.820	115.7±12.7
0.860	125.7±11.9	0.860	118.2±12.0
0.900	149.8±12.0	0.900	140.7±12.0
0.940	164.8±10.6	0.940	153.9±10.7

	501 MeV/c		522 MeV/c
$\lvert\cos\theta^*\rvert$	FDC (μb/sr)	$\lvert\cos\theta^*\rvert$	FDC (μb/sr)
0.025	32.9±7.9	0.025	46.7±8.9
0.075	49.2±9.0	0.075	42.9±8.4
0.125	31.9±8.2	0.125	47.8±9.7
0.175	41.9±8.6	0.175	50.1±9.0
0.225	39.7±8.3	0.225	57.1±10.2
0.275	45.6±9.2	0.275	54.9±10.0
0.325	40.9±8.8	0.325	54.8±10.2
0.375	45.5±9.0	0.375	58.4±10.0
0.425	54.6±9.2	0.425	64.1±10.0
0.475	80.7±11.0	0.475	59.9±9.7
0.525	61.4±9.9	0.525	94.3±12.0
0.575	74.9±10.2	0.575	75.1±10.6
0.625	83.9±10.7	0.625	81.1±10.9
0.675	94.0±10.8	0.675	77.0±10.2
0.725	101.9±11.1	0.725	86.7±10.5
0.775	120.9±11.2	0.775	105.5±11.0
0.820	138.7±13.3	0.820	121.8±12.9
0.860	136.2±12.2	0.860	128.3±12.2
0.900	122.1±10.7	0.900	137.4±11.6
0.940	150.0±10.0	0.940	144.7±10.0

	538 MeV/c		559 MeV/c
$\lvert\cos\theta^*\rvert$	FDC (μb/sr)	$\lvert\cos\theta^*\rvert$	FDC (μb/sr)
0.025	47.7±7.9	0.025	51.9±9.4
0.075	51.3±8.6	0.075	43.7±8.9
0.125	35.8±7.3	0.125	34.2±8.7
0.175	33.4±7.1	0.175	41.5±8.8
0.225	38.4±7.7	0.225	63.6±10.5
0.275	40.7±7.7	0.275	59.0±10.3
0.325	68.4±9.6	0.325	59.5±10.3
0.375	62.6±9.0	0.375	37.3±8.3
0.425	61.9±9.0	0.425	42.5±9.2
0.475	66.7±9.2	0.475	58.1±9.7
0.525	66.5±9.3	0.525	62.7±10.5
0.575	70.0±9.3	0.575	62.7±10.2
0.625	84.1±9.9	0.625	64.8±10.1
0.675	99.2±10.3	0.675	59.5±9.5
0.725	96.5±10.0	0.725	81.4±10.6
0.775	103.9±9.9	0.775	97.7±11.0
0.820	122.8±11.8	0.820	90.2±11.7
0.860	129.8±11.1	0.860	102.6±11.5
0.900	138.6±10.4	0.900	135.2±11.8
0.940	148.3±9.1	0.940	135.5±10.2

	585 MeV/c		628 MeV/c
$\lvert\cos\theta^*\rvert$	FDC (μb/sr)	$\lvert\cos\theta^*\rvert$	FDC (μb/sr)
0.025	27.6±7.1	0.025	39.9±7.8
0.075	42.0±8.0	0.075	49.2±8.6

TABLE III. (*Continued*).

	585 MeV/c		628 MeV/c
$\lvert\cos\theta^*\rvert$	FDC (μb/sr)	$\lvert\cos\theta^*\rvert$	FDC (μb/sr)
0.125	48.4±9.1	0.125	44.3±8.8
0.175	44.2±8.5	0.175	45.5±8.4
0.225	29.7±7.3	0.225	62.2±9.5
0.275	46.5±8.8	0.275	54.9±9.0
0.325	54.4±9.2	0.325	58.6±9.8
0.375	38.4±8.1	0.375	45.1±8.2
0.425	44.1±8.5	0.425	53.8±9.1
0.475	56.6±9.5	0.475	43.1±8.1
0.525	62.0±9.8	0.525	56.8±9.1
0.575	64.3±9.6	0.575	59.6±9.7
0.625	61.0±9.2	0.625	55.7±9.4
0.675	62.3±9.3	0.675	78.5±10.1
0.725	84.3±10.4	0.725	94.7±10.6
0.775	110.4±11.0	0.775	80.2±9.6
0.820	105.7±11.9	0.825	92.3±10.0
0.860	109.2±11.2	0.875	108.7±10.0
0.900	118.5±10.6	0.920	130.2±10.6
0.940	142.8±9.9	0.960	153.2±9.2

	677 MeV/c		718 MeV/c
$\lvert\cos\theta^*\rvert$	FDC (μb/sr)	$\lvert\cos\theta^*\rvert$	FDC (μb/sr)
0.025	36.4±8.7	0.025	48.7±8.8
0.075	57.9±10.1	0.075	39.5±8.3
0.125	49.6±9.7	0.125	39.6±8.7
0.175	38.9±8.9	0.175	54.6±9.3
0.225	37.0±8.5	0.225	46.1±8.5
0.275	63.7±11.2	0.275	26.8±7.0
0.325	59.0±10.6	0.325	50.4±9.6
0.375	45.7±9.7	0.375	32.1±7.5
0.425	42.3±9.6	0.425	57.1±9.6
0.475	55.4±10.1	0.475	51.1±9.1
0.525	59.2±10.5	0.525	47.8±9.0
0.575	53.3±10.0	0.575	49.6±9.2
0.625	47.6±9.3	0.625	55.6±9.5
0.675	85.2±11.6	0.675	53.6±9.1
0.725	69.6±10.5	0.725	86.8±11.3
0.775	91.0±11.3	0.775	88.1±10.8
0.825	97.9±11.5	0.825	112.0±11.4
0.875	133.8±12.0	0.875	122.4±11.1
0.920	133.8±12.1	0.920	138.0±11.5
0.960	152.0±10.3	0.960	158.3±10.2

	756 MeV/c
$\lvert\cos\theta^*\rvert$	FDC (μb/sr)
0.025	48.0±8.1
0.075	37.2±7.6
0.125	52.0±8.8
0.175	36.3±7.6
0.225	32.0±6.8
0.275	41.0±7.9
0.325	48.3±8.6
0.375	50.8±8.6
0.425	50.8±8.4
0.475	48.4±8.4
0.525	43.3±8.0
0.575	41.6±8.0
0.625	66.3±9.4
0.675	78.7±9.7
0.725	71.1±9.4

TABLE III. (*Continued*).

$\lvert\cos\theta^*\rvert$	756 MeV/c FDC (μb/sr)
0.775	86.8±9.8
0.825	112.4±10.6
0.875	146.4±11.3
0.920	141.2±10.7
0.960	149.6±9.1

$\bar{p}p \to \pi^-\pi^+$ events. If a wrong beam momentum was used in the calculation of $\Delta\theta_{\pi\pi}$, the peak position in the $\Delta\theta_{\pi\pi}$ distribution sensitively deviates from 0°. Therefore, the beam momentum at the target center was determined in such a way that the peak position in the $\Delta\theta_{\pi\pi}$ distribution had to be precisely located at 0°. The mass resolution of the $\bar{p}p$ system was determined by the spread of the beam momentum (dominant at higher momenta) and the

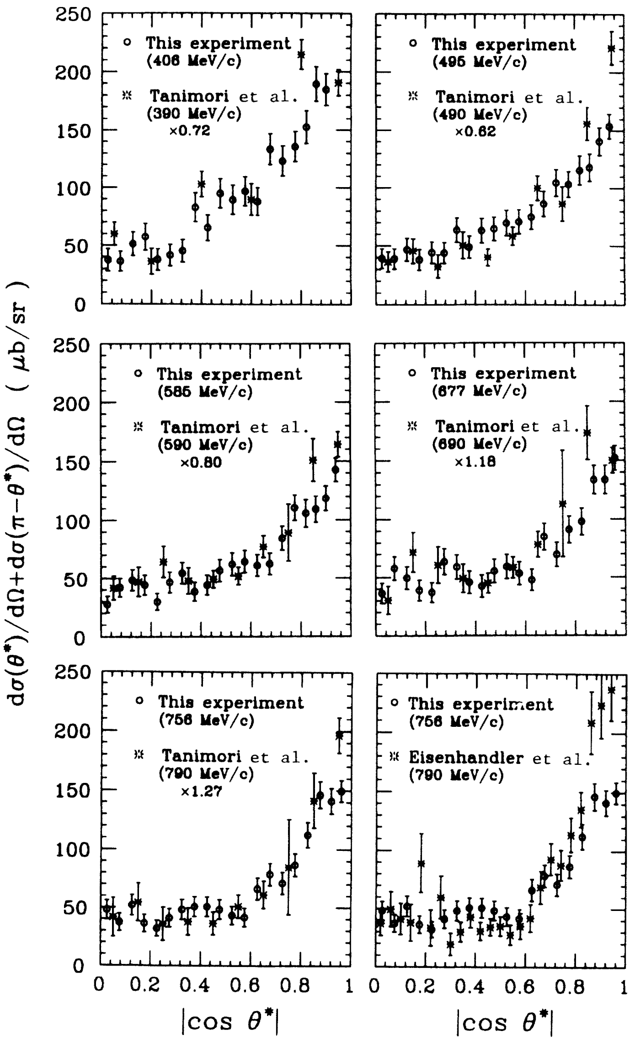

FIG. 13. The folded differential cross sections of the $\bar{p}p \to \pi^-\pi^+$ reaction obtained in this experiment are compared with the ones constructed from the data of Tanimori *et al.* (Ref. 22) and Eisenhandler *et al.* (Ref. 18), which are normalized to the present results with a normalization factor given in each figure.

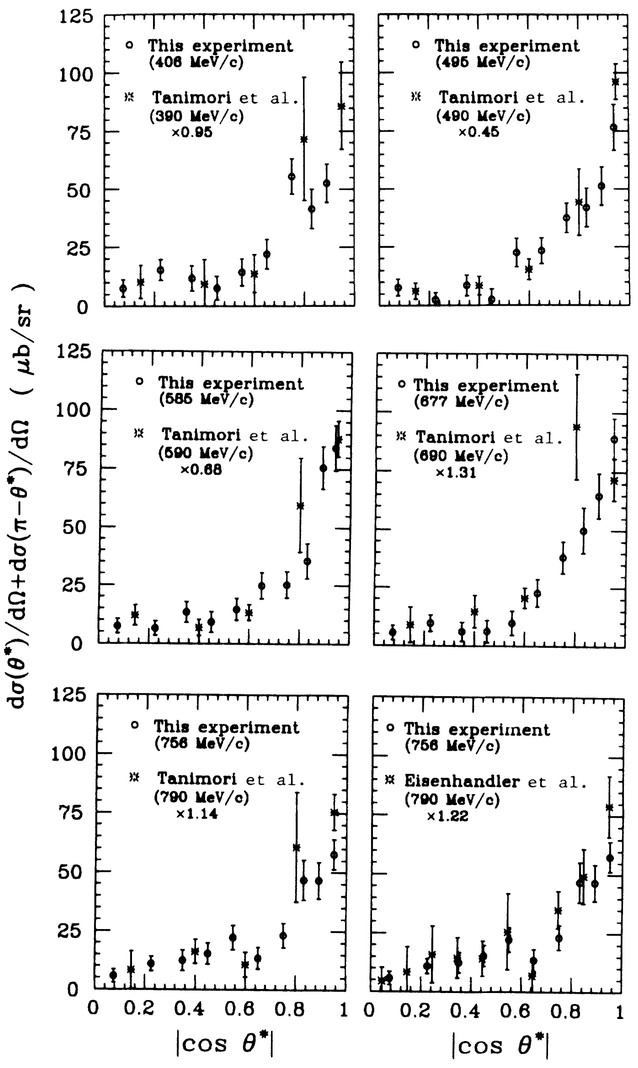

FIG. 14. The folded differential cross sections of the $\bar{p}p \to K^-K^+$ reaction obtained in this experiment are compared with the ones constructed from the data of Tanimori *et al.* (Ref. 22) and Eisenhandler *et al.* (Ref. 18), which are normalized to the present results with a normalization factor given in each figure.

TABLE IV. Folded differential cross sections (FDC) for the $\bar{p}p \to K^-K^+$ reaction.

	362 MeV/c		406 MeV/c
$\|\cos\theta^*\|$	FDC (μb/sr)	$\|\cos\theta^*\|$	FDC (μb/sr)
0.075	23.2±7.3	0.075	7.6±3.7
0.225	10.1±6.8	0.225	15.4±4.4
0.350	9.3±10.1	0.350	11.9±5.3
0.450	4.9±7.0	0.450	7.7±5.0
0.550	29.3±9.9	0.550	14.4±5.7
0.650	5.1±7.7	0.650	22.1±6.3
0.750	21.9±9.0	0.750	55.6±7.6
0.830	17.4±10.7	0.830	41.5±8.5
0.890	62.1±12.7	0.890	52.6±8.3

	447 MeV/c		467 MeV/c
$\|\cos\theta^*\|$	FDC (μb/sr)	$\|\cos\theta^*\|$	FDC (μb/sr)
0.075	11.9±3.8	0.075	2.9±3.1
0.225	17.2±4.2	0.225	7.1±3.3
0.350	10.6±5.2	0.350	11.2±4.9
0.450	15.5±5.1	0.450	14.2±5.0
0.550	24.1±5.7	0.550	5.3±4.4
0.650	26.8±6.1	0.650	26.9±5.9
0.750	29.2±5.9	0.750	28.4±6.0
0.825	46.4±10.2	0.825	48.8±10.0
0.875	44.4±8.5	0.875	48.1±9.3
0.920	58.0±9.2	0.920	64.0±9.4

	482 MeV/c		495 MeV/c
$\|\cos\theta^*\|$	FDC (μb/sr)	$\|\cos\theta^*\|$	FDC (μb/sr)
0.075	15.9±4.0	0.075	7.7±3.5
0.225	4.8±3.3	0.225	2.4±3.0
0.350	13.9±4.8	0.350	8.5±4.4
0.450	0.0±3.8	0.450	2.5±4.4
0.550	15.5±5.6	0.550	22.4±6.0
0.650	22.2±5.6	0.650	23.2±5.5
0.750	42.7±6.4	0.750	37.4±6.4
0.830	47.3±8.7	0.830	41.9±8.4
0.890	58.3±8.7	0.890	51.3±8.2
0.940	77.6±9.2	0.940	76.6±9.9

	501 MeV/c		522 MeV/c
$\|\cos\theta^*\|$	FDC (μb/sr)	$\|\cos\theta^*\|$	FDC (μb/sr)
0.075	3.2±3.2	0.075	16.4±4.1
0.225	13.0±3.8	0.225	9.8±3.4
0.350	8.3±4.5	0.350	12.5±5.0
0.450	3.9±4.4	0.450	11.2±4.6
0.550	10.1±4.9	0.550	11.2±4.9
0.650	20.2±5.2	0.650	33.0±6.4
0.750	31.5±5.9	0.750	37.8±6.4
0.830	46.6±8.5	0.830	63.0±9.5
0.890	59.5±8.3	0.890	66.6±8.7
0.940	81.3±9.4	0.940	65.7±9.2

	538 MeV/c		559 MeV/c
$\|\cos\theta^*\|$	FDC (μb/sr)	$\|\cos\theta^*\|$	FDC (μb/sr)
0.075	10.2±3.2	0.075	10.1±3.5
0.225	15.5±3.7	0.225	8.2±3.5
0.350	3.2±3.5	0.350	12.0±4.8
0.450	7.9±3.9	0.450	18.3±5.4
0.550	9.0±4.3	0.550	24.3±6.1
0.650	14.6±4.6	0.650	28.3±6.1

TABLE IV. (*Continued*).

	538 MeV/*c*		559 MeV/*c*
$\lvert\cos\theta^*\rvert$	FDC (μb/sr)	$\lvert\cos\theta^*\rvert$	FDC (μb/sr)
0.750	28.5±5.4	0.750	35.1±6.4
0.830	44.2±7.8	0.830	45.4±9.0
0.890	60.1±7.6	0.890	50.1±8.2
0.940	76.5±8.4	0.940	72.6±9.8

	585 MeV/*c*		628 MeV/*c*
$\lvert\cos\theta^*\rvert$	FDC (μb/sr)	$\lvert\cos\theta^*\rvert$	FDC (μb/sr)
0.075	7.4±3.1	0.075	6.9±3.0
0.225	6.5±3.0	0.225	10.7±3.4
0.350	13.4±4.4	0.350	7.0±3.9
0.450	9.2±4.4	0.450	9.7±4.1
0.550	14.6±4.7	0.550	9.9±4.3
0.650	24.8±5.6	0.650	23.4±5.5
0.750	25.2±5.7	0.750	36.8±6.2
0.830	35.5±7.6	0.830	42.6±8.7
0.890	75.7±9.0	0.890	37.7±7.6
0.940	84.1±9.6	0.950	70.6±6.9

	677 MeV/*c*		718 MeV/*c*
$\lvert\cos\theta^*\rvert$	FDC (μb/sr)	$\lvert\cos\theta^*\rvert$	FDC (μb/sr)
0.075	5.5±3.1	0.075	5.9±3.0
0.225	9.6±3.5	0.225	9.7±3.3
0.350	6.0±4.0	0.350	14.1±4.8
0.450	6.2±4.7	0.450	18.8±5.1
0.550	9.8±5.2	0.550	17.5±5.4
0.650	22.7±5.9	0.650	18.2±5.4
0.750	38.1±6.9	0.750	31.3±6.1
0.830	49.9±9.9	0.830	49.1±9.1
0.890	64.8±9.6	0.890	63.4±9.3
0.950	89.1±8.6	0.950	61.0±7.1

	756 MeV/*c*
$\lvert\cos\theta^*\rvert$	FDC (μb/sr)
0.075	5.7±2.8
0.225	10.9±3.2
0.350	12.4±4.4
0.450	15.4±4.5
0.550	22.3±5.2
0.650	13.5±4.7
0.750	23.2±5.2
0.830	46.8±8.5
0.890	46.6±7.7
0.950	57.7±6.3

energy loss in the liquid-hydrogen target (dominant at lower momenta). The beam momentum at the center of the liquid-hydrogen target and the mass resolution at each beam momentum are given in Table II together with some other relevant parameters.

IV. RESULTS AND DISCUSSION

A. Experimental results

The folded differential cross section for the *i*th subdivision of $|\cos\theta^*|$ is given by

$$\frac{d\sigma}{d\Omega}(\theta_i^*)+\frac{d\sigma}{d\Omega}(\pi-\theta_i^*)=\frac{N_i}{\Omega_i N_{\bar{p}} N_p \epsilon}\ ,$$

where N_i and Ω_i are the number of events and the solid-angle acceptance corresponding to the *i*th subdivision, $N_{\bar{p}}$ is the number of the beam antiprotons, N_p is the number of the target protons, and ϵ is the total efficiency calculated from the efficiencies given in Table I. The solid-angle acceptance Ω_i is defined as an average of $\Omega(\theta_i^*)$ and $\Omega(\pi-\theta_i^*)$.

The cross sections have been determined over the $|\cos\theta^*|$ region where the two peaks corresponding to the

TABLE V. Legendre coefficients and the value of the reduced χ^2 ($\chi^2/N_{\rm DF}$) of the fit to the $\bar{p}p\to\pi^-\pi^+$ folded differential cross section, where $N_{\rm DF}$ is the number of degrees of freedom. Note that $2\pi a_0$ in the second column gives $\sigma_{\pi^-\pi^+}$.

$P_{\rm lab}$ (MeV/c)	$2\pi a_0$(μb)	a_2/a_0	a_4/a_0	a_6/a_0	$\chi^2/N_{\rm DF}$
362	617±27	1.27±0.13	−0.21±0.17		1.18
406	613±18	1.26±0.09	0.07±0.12		1.07
447	546±17	1.15±0.09	0.07±0.14	0.12±0.15	0.60
467	522±16	1.21±0.10	0.25±0.14	0.24±0.15	1.25
482	507±15	1.16±0.07	0.17±0.11	0.15±0.13	0.97
495	489±15	1.07±0.08	0.17±0.12	0.10±0.14	0.27
501	484±14	1.09±0.07	−0.07±0.11	−0.16±0.14	0.71
522	504±15	0.93±0.07	0.18±0.11	0.09±0.13	0.47
538	495±13	1.04±0.07	0.08±0.10	0.03±0.12	0.79
559	440±14	0.96±0.08	0.40±0.12	0.06±0.15	0.98
585	428±13	1.11±0.08	0.27±0.12	0.02±0.14	0.93
628	442±13	0.94±0.07	0.45±0.10	0.10±0.12	0.77
677	439±14	1.03±0.08	0.48±0.11	0.01±0.14	1.03
718	423±13	1.16±0.08	0.55±0.11	−0.09±0.13	0.99
756	431±12	1.16±0.07	0.45±0.10	−0.14±0.12	1.08

$\pi^-\pi^+$ and K^-K^+ events are well separated in the $R_{\pi K}$ distribution (more than 3σ where σ is the one-standard-deviation width of the $\pi^-\pi^+$ and K^-K^+ peaks). The region of $|\cos\theta^*|$ varies from $|\cos\theta^*|<0.92$ at 362 MeV/c to $|\cos\theta^*|<0.98$ at 756 MeV/c.

The results are given in Table III for the $\bar{p}p\to\pi^-\pi^+$ reaction and Table IV for the $\bar{p}p\to K^-K^+$ reaction together with their statistical errors, and are also plotted in Figs. 11 and 12, respectively. In Figs. 13 and 14 the folded differential cross sections obtained in this experiment are compared with those obtained by Tanimori *et al.*[22] and by Eisenhandler *et al.*[18] at several beam momenta, where the data from other experiments[18,22] are normalized to our data with the normalization constant given in each figure. This comparison indicates that our data and those from Refs. 18 and 22 show agreement with respect to the shape of the folded angular distributions in both $\pi^-\pi^+$ and K^-K^+ channels. This seems to suggest that an enhancement reported by Tanimori *et al.*[22] in the $\pi^-\pi^+$ and K^-K^+ channels at 490 MeV/c is due to statistical fluctuation or some normalization problem.

The folded differential cross sections were fitted with Legendre polynomials of the form

$$\frac{d\sigma}{d\Omega}(\theta^*)+\frac{d\sigma}{d\Omega}(\pi-\theta^*)=\sum_{n=0}^{n_{\max}} a_n P_n(\cos\theta^*)\ , \qquad n=\text{even}\ .$$

The odd-order terms do not contribute to the folded differential cross section. For the $\pi^-\pi^+$ channel, the fit was performed with $n_{\max}=4$ at 362 and 406 MeV/c and

TABLE VI. Legendre coefficients, and the value of reduced χ^2 ($\chi^2/N_{\rm DF}$) of the fit to the $\bar{p}p\to K^-K^+$ folded differential cross sections, where $N_{\rm DF}$ is the number of degrees of freedom. Note that $2\pi a_0$ in the second column gives $\sigma_{K^-K^+}$.

$P_{\rm lab}$ (MeV/c)	$2\pi a_0$(μb)	a_2/a_0	a_4/a_0	$\chi^2/N_{\rm DF}$
362	134±20	1.44±0.44	1.65±0.58	1.68
406	160±13	1.73±0.26	0.16±0.32	1.98
447	161±12	1.30±0.21	0.44±0.28	0.44
467	135±11	2.09±0.25	0.76±0.30	1.12
482	155±11	2.07±0.19	1.15±0.25	2.07
495	141±11	2.18±0.21	0.74±0.28	1.15
501	145±11	2.24±0.21	1.14±0.26	0.82
522	174±11	1.73±0.18	0.80±0.23	1.26
538	145±10	2.04±0.19	1.46±0.23	0.64
559	164±11	1.59±0.19	0.33±0.25	0.33
585	154±11	2.08±0.19	1.05±0.24	1.37
628	136±10	1.87±0.18	0.78±0.23	1.10
677	156±11	2.27±0.19	1.12±0.23	0.28
718	150±10	1.69±0.17	0.45±0.22	0.75
756	133±9	1.61±0.18	0.55±0.23	1.23

$n_{\max}=6$ at higher beam momenta, with the results given in Table V. It is seen that the resulting coefficient of the highest-order term is consistent with 0. For the K^-K^+ channel, the fit was performed with $n_{\max}=4$ at all the beam momenta since the fit with $n_{\max}=6$ not only resulted in a_6 consistent with 0, but also caused oscillation of the fitted curve around $|\cos\theta^*|\sim 1$ at several beam momenta. The results are given in Table VI. The curves in Figs. 11 and 12 show the results of the fit.

The total cross sections $\sigma_{\pi^-\pi^+}$ and $\sigma_{K^-K^+}$ of the reactions $\bar{p}p\rightarrow\pi^-\pi^+$ and K^-K^+ are obtained by integrating the folded differential cross sections from $\cos\theta^*=0$ to 1, which is equal to $2\pi a_0$ and listed in the second column of Tables V and VI. The cross sections $\sigma_{\pi^-\pi^+}$ and $\sigma_{K^-K^+}$ as a function of the incident $\bar{p}$ momentum are plotted in Fig. 15 together with the data from other experiments.[17-23] The error bars show statistical errors only. Both $\sigma_{\pi^-\pi^+}$ and $\sigma_{K^-K^+}$ measured in this experiment show smooth momentum dependence; $\sigma_{\pi^-\pi^+}$ smoothly decreases with beam momentum up to 550 MeV/c and then levels off, while $\sigma_{K^-K^+}$ is nearly constant over the beam momentum region investigated in this experiment.

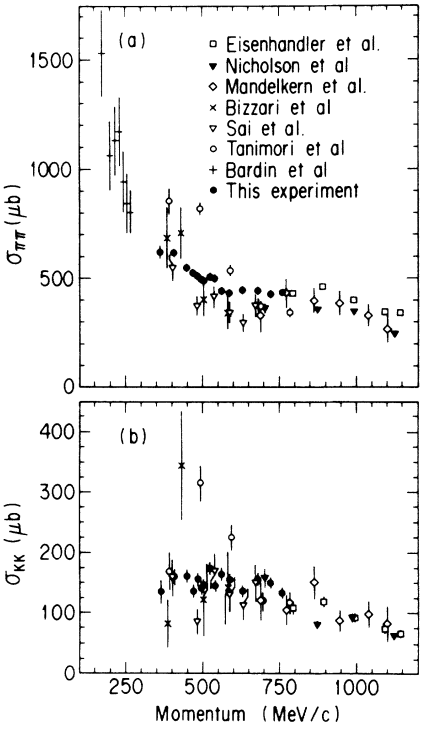

FIG. 15. (a) Total cross section for the $\bar{p}p\rightarrow\pi^-\pi^+$ reaction plotted as a function of incident beam momentum. The data from other experiments are also shown. (b) Total cross section for the $\bar{p}p\rightarrow K^-K^+$ reaction plotted as a function of incident beam momentum. The data from other experiments are also shown.

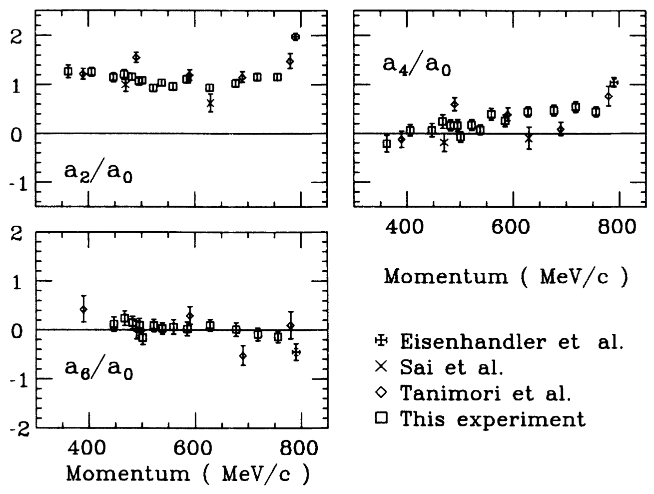

FIG. 16. Legendre coefficients for the $\bar{p}p\rightarrow\pi^-\pi^+$ reaction as a function of incident beam momentum. The data from other experiments are also shown.

The normalized Legendre coefficients (a_n/a_0) are plotted together with the results obtained in other experiments[18,21,22] in Fig. 16 for $\pi^-\pi^+$ and Fig. 17 for K^-K^+ as a function of the beam momentum. Our results are consistent with the results of other experiments.[18,21,22] This again indicates that the shapes of the folded angular distributions obtained in this experiment are consistent with those obtained in other experiments.[18,21,22]

In the $\pi^-\pi^+$ channel, a_4 increases slowly and smoothly as the beam momentum increases, while a_2 is nearly constant over the beam momentum region investigated in this experiment. In particular, a_4 is consistent with zero below 400 MeV/c.

In the K^-K^+ channel, both a_2 and a_4 are large and nearly constant ($a_2/a_0\sim 2$ and $a_4/a_0\sim 1$). These a_2 and a_4 contributions produce large forward and backward symmetric peaks, unless there are large a_1 and/or a_3 contributions. Although a_1 and a_3 are not obtained in this experiment the results obtained in other experiments[18,21,22] show that both a_1/a_0 and a_3/a_0 are nega-

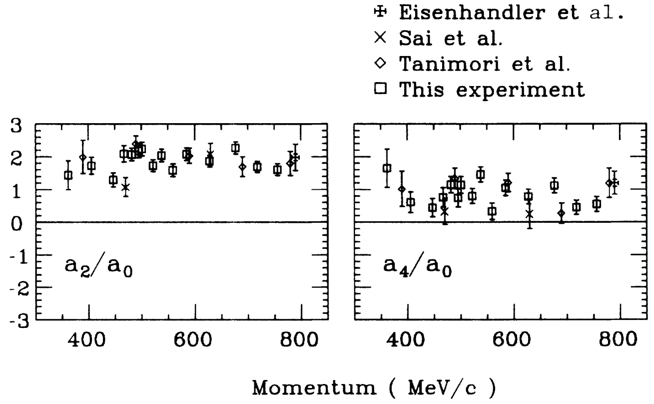

FIG. 17. Legendre coefficients for the $\bar{p}p\rightarrow K^-K^+$ reaction as a function of incident beam momentum. The data from other experiments are also shown.

tive and nearly constant ($a_1/a_0 \sim -0.6$ and $a_3/a_0 \sim -1$). These a_1 and a_3 contributions are insufficient to cancel out the prominent backward peak produced by a_2 and a_4.

As mentioned in Sec. I, the existence of the backward peak in the K^-K^+ angular distribution at low energies is an important problem. In the following, some comments are in order on this K^-K^+ backward peak. At $P_{\rm lab}=790$ MeV/c, Eisenhandler *et al.*[18] and Tanimori *et al.*[22] gave the complete K^-K^+ angular distributions, both results being in good agreement and indicating a prominent backward peak. Below 700 MeV/c Tanimori *et al.*[22] provided the K^-K^+ angular distribution with good statistics, and indicated the existence of a steep backward peak. Unfortunately, the data of Ref. 22 have a normalization problem as has been described above. However, it seems that the data of Ref. 22, properly normalized to the folded differential cross sections obtained in this experiment, give correct differential cross sections for the $\pi^-\pi^+$ and K^-K^+ channels which can be directly compared with theoretical calculations.

B. Comparison with theoretical model calculations

There are several calculations for the $\bar{p}p\to\pi^-\pi^+$ and K^-K^+ cross sections below 1 GeV/c based on theoretical models for these reactions. Here we compare our results with the predictions of these theoretical calculations to test the validity of the adopted models.

Kohno and Weise[12] calculated the relevant cross sections and angular distributions employing a nonrelativistic quark model (hereafter this model is abbreviated as the KW model). The transition potentials corresponding to the R and A processes have been derived from the gluon-exchange picture. It is claimed that this approach is less restrictive than the $^3P_0$ model in which a quark and an antiquark annihilate into the vacuum quantum number. In this model both the R process [Fig. 1(a)] and the A process [Fig. 1(b)] contribute nearly equally to the $\pi^-\pi^+$ channel in this momentum region. Figure 18 shows a comparison of the present data with the predictions by the KW model. Also, the angular distributions of Tanimori *et al*,[22] normalized to the present data are compared in Fig. 19 with the predictions of the KW model. From these figures it is seen that the KW model reproduces rather well the gross features of the $\bar{p}p\to\pi^+\pi^+$ angular distributions. However, this model completely fails to reproduce the forward and, in particular, the steep backward peaks characteristic of the $\bar{p}p\to K^-K^+$ reaction in the low-momentum region. Moreover, their prediction for the momentum dependence of both $\sigma_{\pi^-\pi^+}$ and $\sigma_{K^-K^+}$ shows a steep decrease with increasing momentum, and this feature is in disagreement with our data as shown in Fig. 20.

Maruyama and Ueda[5] also made calculations for low-energy $\bar{p}p\to\pi^-\pi^+$ and K^-K^+ cross sections based on a nonrelativistic quark model (hereafter abbreviated as the MU model). In their model two types of the gluon-exchange diagrams called $A_{\rm I}$ and $A_{\rm II}$ processes (see Fig. 21) are explicitly taken into account for the A process (in the KW model, only one type of gluon-exchange diagram $A_{\rm II}$ is considered). In Fig. 20 the contributions to $\sigma_{\pi^-\pi^+}$ and $\sigma_{K^-K^+}$ from each component of the initial orbital angular momentum state L and their incoherent sum are shown as a function of the incident beam momentum. The $L=2$ component increases with the beam momentum and dominates both $\sigma_{\pi^-\pi^+}$ and $\sigma_{K^-K^+}$ above $\sim$500 MeV/c. In the MU model the R process gives only a small contribution to the $\bar{p}p\to\pi^-\pi^+$ reaction, and above $\sim$600 MeV/c the $L=2$ component itself is dominated by the $A_{\rm I}$ process. Therefore, the incoherent summation of the different L contributions may be justified above $\sim$600 MeV/c. Indeed, the incoherent sum shows agreement with the $\bar{p}p\to\pi^-\pi^+$ data only above $\sim$550 MeV/c.

The angular distributions predicted by the MU model for both $\pi^-\pi^+$ and K^-K^+ channels at 590 MeV/c are compared with the present data and with the data of Tanimori *et al.*[22] properly normalized to the present data in Figs. 18 and 19, respectively. The gross behavior of

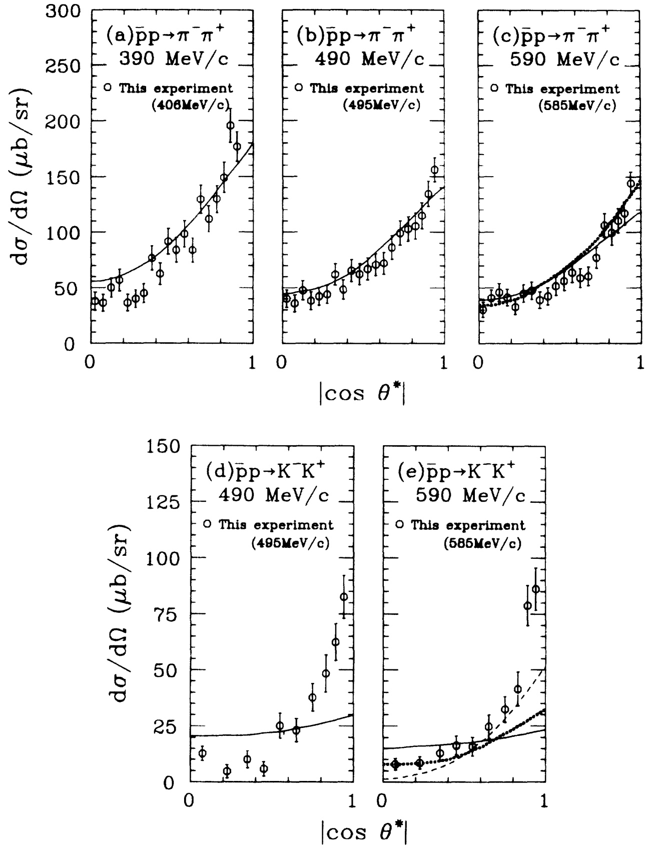

FIG. 18. The folded differential cross sections obtained in this experiment are compared with the results of theoretical calculations for (a)–(c) the $\bar{p}p\to\pi^-\pi^+$ reaction and (d), (e) the $\bar{p}p\to K^-K^+$ reaction. The solid curves show the prediction by the KW model. The dotted curve in (c) shows the prediction by the MU model. The dotted curve in (e) shows the $L=2$ contribution, and the dashed curve in (e) shows the result of the maximum destructive interference between the $L=0$ and $L=2$ contributions, both predicted by the MU model.

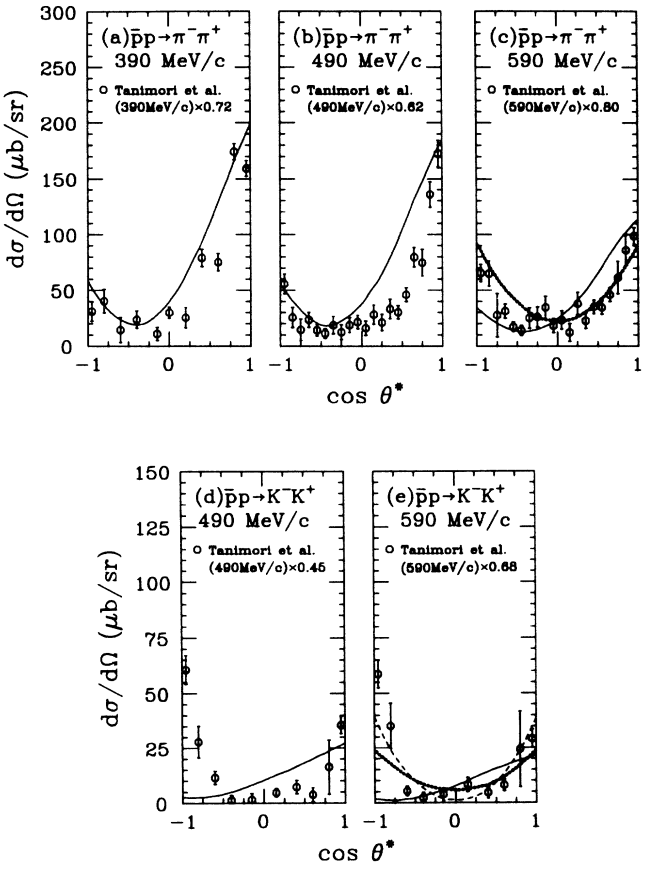

FIG. 19. The differential cross sections of Tanimori *et al.* (Ref. 22) normalized to the present data are compared with the results of theoretical calculations for (a)–(c) the $\bar{p}p \to \pi^-\pi^+$ reaction and (d), (e) the $\bar{p}p \to K^-K^+$ reaction. The solid curves show the prediction by the KW model. The dotted curve in (c) shows the prediction by the MU model. The dotted curve in (e) shows the $L=2$ contribution, and the dashed curve in (e) shows the result of the maximum destructive interference between the $L=0$ and $L=2$ contributions, both predicted by the MU model.

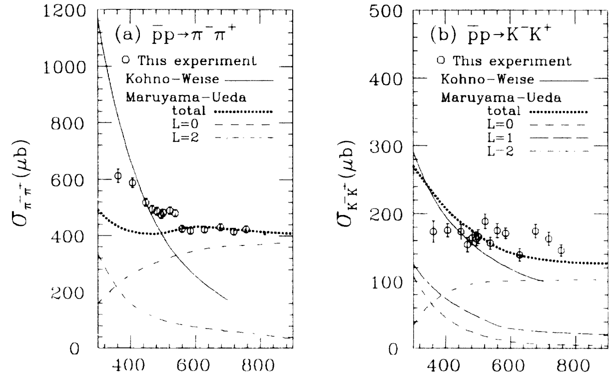

FIG. 20. Total cross sections obtained in this experiment are compared with the theoretical calculations by the KW model and by the MU model for (a) the $\bar{p}p \to \pi^-\pi^+$ reaction and (b) the $\bar{p}p \to K^-K^+$ reaction. For the MU model, the $L=0$, 1, and 2 contributions and the summed contribution are separately shown.

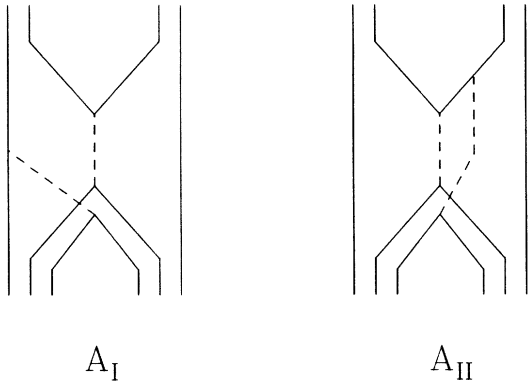

FIG. 21. Diagrams for (a) A_{I} quark-annihilation process and (b) A_{II} quark-annihilation process considered by Maruyama and Ueda.

angular distribution for the $\pi^-\pi^+$ channel is well reproduced. For the K^-K^+ channel the forward and backward peaks appear due to the dominance of the $L=2$ component above 500 MeV/*c*. However, this $L=2$ contribution does not fit the data even in the forward region. Even if the maximum destructive interference between the $L=0$ and $L=2$ components are taken into account, no satisfactory fit is obtained in the backward region, though the forward peak is now reproduced. It should also be noted that the prominent forward and backward peaks appear already at around 400 Mev/*c* in the data of Tanimori *et al.*[22] In the MU model, however, it seems difficult to explain this feature, because the $L=2$ contribution is not yet dominant around 400 MeV/*c* as shown in Fig. 20.

Another theoretical calculation has been performed by Moussallam for the $\pi^-\pi^+$ channel[30,31] and for the K^-K^+ channel[32] based on a baryon-exchange potential model. His results on the angular distribution for the $\pi^-\pi^+$ channel reproduce the experimental data with the forward and backward peaks. However, the results on the angular distribution for the K^-K^+ channel show a forward peak but no backward peak, in contradiction to the experimental data.[18,22]

The discussion above is summarized as follows. (i) The momentum dependence of $\sigma_{\pi^-\pi^+}$ and $\sigma_{K^-K^+}$ is not completely explained by theoretical calculations in the full momentum region investigated in the present experiment. (ii) The angular distribution of the $\bar{p}p \to \pi^-\pi^+$ reaction is reproduced by theoretical calculations. However, that of the $\bar{p}p \to K^-K^+$ reaction cannot be reproduced at all. In particular, the prominent backward peak observed in $\bar{p}p \to K^-K^+$ is most difficult to explain.

As already noted in Sec. I the recent European Muon Collaboration (EMC) experiment of deep-inelastic muon-proton scattering[14] suggests that the proton contains a significant amount of $s\bar{s}$ pairs.[33] Then, intuitively, the diagram shown in Fig. 1(c) may produce the backward peak in the $\bar{p}p \to K^-K^+$ reaction as pointed out by Ellis, Gabathuler, and Karliner.[16] Explicit theoretical calculations of the $\bar{p}p \to K^-K^+$ angular distribution including this diagram, however, have to be done to see whether it really produces the necessary amount of the backward peak.

V. CONCLUSIONS

We have presented the folded differential cross sections and the total cross sections of both $\bar{p}p \to \pi^-\pi^+$ and K^-K^+ reactions at 15 incident beam momenta between 360 and 760 MeV/c with much higher statistics and much smaller systematic errors than those in previous experiments. The high statistics and the fineness of the momentum step enabled us to make detailed comparison of the experimental data with the results of theoretical calculations.

The shapes of the folded angular distributions obtained in this experiment are consistent with those constructed from the data of the previous measurements, and are characterized by a prominent peak at $|\cos\theta^*|=1$. The Legendre polynomial series of up to the fourth or sixth order for the $\pi^-\pi^+$ channel and up to the fourth order for the K^-K^+ channel give satisfactory fits to the folded angular distributions. This suggests that only lower partial waves are dominant in this momentum region. By comparing the present data with that of Tanimori *et al.*,[22] the data reported in Ref. 22 are found to have a normalization problem at some beam momenta, and those properly normalized to the present data are considered to give the correct differential cross sections.

The total $\bar{p}p \to \pi^-\pi^+$ and K^-K^+ cross sections $\sigma_{\pi^-\pi^+}$ and $\sigma_{K^-K^+}$, respectively, have been obtained from the zeroth-order coefficients of the Legendre polynomial fit to the folded differential cross sections. The present results exhibit a smooth but rapidly decreasing behavior of $\sigma_{\pi^-\pi^+}$ as the beam momentum increases up to 550 MeV/c, and a smooth and nearly constant momentum dependence of $\sigma_{K^-K^+}$.

The present results have been compared with the theoretical calculations by Kohno and Weise[12] and by Maruyama and Ueda,[5] both based on a nonrelativistic quark model, and by Moussallam[30–32] based on a baryon-exchange potential model. Although the gross shape of the angular distribution of the reaction $\bar{p}p \to \pi^-\pi^+$ is reproduced by these theoretical calculations, the prominent backward peak (or peak at $|\cos\theta^*|=1$) in the $\bar{p}p \to K^-K^+$ reaction cannot be explained at all. It should be noted also that the momentum dependence of $\sigma_{\pi^-\pi^+}$ and $\sigma_{K^-K^+}$ is not completely explained by theoretical calculations. These facts seem to suggest that something important is still missing in the theoretical models for the $\bar{p}p \to \pi^-\pi^+$ and K^-K^+ reactions. In this regard the recent proposal by Ellis, Gabathular, and Karliner[16] is very interesting. Based on the recent EMC results[14] which indicate the existence of a significant amount of $\bar{s}s$ pairs in the proton, they have pointed out the possibility that the new quark diagram shown in Fig. 1(c) gives the backward peak in the $\bar{p}p \to K^-K^+$ reaction.[33] Theoretical calculations of the $\bar{p}p \to K^-K^+$ differential cross section including this diagram, however, remain to be done.

ACKNOWLEDGMENTS

We would like to thank the staff of the KEK accelerator department for the excellent machine operation and the staff of the KEK experiment supporting group for their help. Thanks are also due to Dr. Y. Takada and Mr. S. Kasai who participated in the early phase of this experiment. One of us (T.T.) wishes to acknowledge fruitful discussion with Professor T. Ueda.

---

*Present address: Institute for Cosmic Ray Research, University of Tokyo, Tanashi, Tokyo 188, Japan.

†Present address: Tsukuba Institute of Science and Technology, Tsuchiura, Ibaraki 300, Japan.

‡Present address: National Laboratory for High Energy Physics, Oho, Ibaraki 305, Japan.

§Present address: Y-S-Technosystem Ltd., Hikaricho, Higashi-ku, Hiroshima 732, Japan.

[1] M. Maruyama and T. Ueda, Nucl. Phys. **A364**, 297 (1981).

[2] M. Maruyama and T. Ueda, Prog. Theor. Phys. **73**, 1211 (1985).

[3] M. Maruyama and T. Ueda, Prog. Theor. Phys. **74**, 526 (1985).

[4] M. Maruyama, S. Furui, and A. Faessler, Nucl. Phys. **A472**, 643 (1987).

[5] M. Maruyama and T. Ueda, Prog. Theor. Phys. **78**, 841 (1987).

[6] S. Furui, A. Faessler, and S. B. Khadkikar, Nucl. Phys. **A424**, 495 (1984); S. Furui and A. Faessler, *ibid.* **A424**, 525 (1984).

[7] C. B. Dover and P. M. Fishbane, Nucl. Phys. **B244**, 349 (1984).

[8] C. B. Dover, P. M. Fishbane, and S. Furui, Phys. Rev. Lett. **57**, 1538 (1986).

[9] A. M. Green, J. A. Niskanen, and S. Wycech, Phys. Lett. **139B**, 15 (1984).

[10] U. Hartmann, E. Klempt, and J. G. Korner, Phys. Lett. **155B**, 163 (1985).

[11] J. A. Niskanen and F. Myhrer, Phys. Lett. **157B**, 247 (1985).

[12] M. Khono and W. Weise, Nucl. Phys. **A454**, 429 (1986).

[13] E. M. Henley, T. Oka, and J. Vergados, Phys. Lett. **166B**, 274 (1986).

[14] J. Ashman *et al.*, Phys. Lett. B **206**, 364 (1988).

[15] S. J. Brodsky, J. Ellis, and M. Karliner, Phys. Lett. B **206**, 309 (1988).

[16] J. Ellis, E. Gabathuler, and M. Karliner, Phys. Lett. B **217**, 173 (1989).

[17] H. Nicholson *et al.*, Phys. Rev. D **7**, 2572 (1973).

[18] E. Eisenhandler *et al.*, Nucl. Phys. **B96**, 109 (1975).

[19] R. Bizzarri *et al.*, Lett. Nuovo Cimento **1**, 749 (1969).

[20] M. A. Mandelkern *et al.*, Phys. Rev. D **4**, 2658 (1971).

[21] F. Sai *et al.*, Nucl. Phys. **B213**, 371 (1983).

[22] T. Tanimori *et al.*, Phys. Rev. Lett. **55**, 1835 (1985); T. Tanimori, Ph.D. thesis, University of Tokyo, 1985.

[23] G. Bardin *et al.*, Phys. Lett. B **192**, 471 (1987).

[24] Y. Sugimoto *et al.*, Phys. Rev. D **37**, 583 (1988).

[25] M. Takasaki *et al.*, Nucl. Instrum. Methods **242**, 201 (1986).

[26] T. Kageyama *et al.*, Jpn. J. Appl. Phys. **24**, 1522 (1985).

[27] Y. Sugimoto, Ph.D. thesis, Kyoto University, 1988; M. Sudou, Ph.D. thesis, University of Tokyo, 1989.

[28] M. Ikeno *et al.*, Nucl. Instrum. Methods **225**, 347 (1984).

[29] D. G. Cassel and H. Kowalski, Nucl. Instrum. Methods **185**,

235 (1981).

[30] B. Moussallam, Nucl. Phys. **A407**, 413 (1983).

[31] B. Moussallam, Nucl. Phys. **A429**, 429 (1984).

[32] B. Moussallam, in *Physics with Antiprotons at LEAR in the ACOL Era,* proceedings of the Third LEAR Workshop, Tignes, Savoie, France, 1985, edited by U. Gastaldi, R. Klapisch, J. M. Richard, and J. Tran Thanh Van (Editions Frontières, Gif-sur-Yvette, 1985), p. 203.

[33] Whether the EMC results imply a significant admixture of the $s\bar{s}$ pair in the proton even at a small momentum transfer, however, is subject to some controversy, and there is considerable criticism about the proposal by Ellis, Gabathular, and Karliner (Ref. 16). See, for example, C. B. Dover and P. M. Fishbane, Phys. Rev. Lett. **62**, 2917 (1989); H. J. Lipkin, Phys. Lett. B **225**, 287 (1989).